



HAL
open science

Pentagonal Bipyramidal Ln(III) Complexes Containing an Axial Phosphine Oxide Ligand: Field-induced Single-ion Magnetism Behavior of the Dy(III) Analogues

Pankaj Kalita, Naushad Ahmed, Arun Kumar Bar, Sourav Dey, Anukul Jana, Gopalan Rajaraman, Jean-Pascal Sutter, Vadapalli Chandrasekhar

► **To cite this version:**

Pankaj Kalita, Naushad Ahmed, Arun Kumar Bar, Sourav Dey, Anukul Jana, et al.. Pentagonal Bipyramidal Ln(III) Complexes Containing an Axial Phosphine Oxide Ligand: Field-induced Single-ion Magnetism Behavior of the Dy(III) Analogues. *Inorganic Chemistry*, 2020, 59 (9), pp.6603-6612. 10.1021/acs.inorgchem.0c00751 . hal-02565216

HAL Id: hal-02565216

<https://hal.science/hal-02565216>

Submitted on 10 Nov 2020

HAL is a multi-disciplinary open access archive for the deposit and dissemination of scientific research documents, whether they are published or not. The documents may come from teaching and research institutions in France or abroad, or from public or private research centers.

L'archive ouverte pluridisciplinaire **HAL**, est destinée au dépôt et à la diffusion de documents scientifiques de niveau recherche, publiés ou non, émanant des établissements d'enseignement et de recherche français ou étrangers, des laboratoires publics ou privés.

**Pentagonal Bipyramidal Ln(III) Complexes Containing an Axial Phosphine Oxide
Ligand: Field-induced Single-ion Magnetism Behavior of the Dy(III) Analogues**

*Pankaj Kalita,^{a,b} Naushad Ahmed,^{‡b} Arun Kumar Bar,^a Sourav Dey,^{‡c} Anukul Jana,^b Gopalan Rajaraman^{*c}, Jean-Pascal Sutter^{*d} and Vadapalli Chandrasekhar^{*b,e}*

^aSchool of Chemical Sciences, National Institute of Science Education and Research, HBNI, Bhubaneswar -752050, India.

^bTata Institute of Fundamental Research Hyderabad, Gopanally, Hyderabad-500107, India.

^cDepartment of Chemistry, Indian Institute of Technology Bombay, Mumbai-400 076, India

^d Laboratoire de Chimie de Coordination du CNRS (LCC-CNRS),, Université de Toulouse, CNRS, Toulouse, France.

^eDepartment of Chemistry, IIT Kanpur, Kanpur 208016, India.

*vc@tifrh.res.in; vc@iitk.ac.in; sutter@lcc-toulouse.fr; rajaraman@chem.iitb.ac.in

[‡]Authors contributed equally in this manuscript

Abstract

A series of neutral homologous complexes [(L)Ln(Cy₃PO)Cl] {where Ln = Gd (**1**), Tb (**2**), Dy (**3**) and Er (**5**)} and [(L)Dy(Ph₃PO)Cl] (**4**) [H₂L = 2,6-diacetylpyridine *bis*-benzoylhydrazone] have been isolated. In these complexes, the central lanthanide ion possesses a pentagonal bipyramidal (PBP) geometry with an overall pseudo D_{5h} symmetry. The coordination environment around the lanthanide ion comprises of three nitrogen and two oxygen donors in an equatorial plane. The axial positions are taken up by a phosphine oxide (O donor) and a chloride ion. Among these compounds, the Dy(III) (**3** and **4**) analogues were found to be field-induced single-ion magnets.

Introduction

There has been a significant renaissance in the chemistry of the *rare earth* elements because of their applications in catalysis¹, photophysical properties² and in magnetic materials³. In recent years lanthanide⁴ and some actinide complexes⁵ are finding increasing utility as molecular magnets (single-molecule- and single-ion magnets; SMMs and SIMs). These molecular systems, once magnetized, retain their magnetization even after the removal of the external magnetic field and are characterized by a slow reversal of magnetization below certain temperatures.⁶ This is because in SMMs, on application of a magnetic field, a double-well potential comprising of the various m_j or m_s states with an energy barrier (U_{eff}) is generated which prevents the reversal of magnetization below certain temperatures (the blocking temperature, T_B).⁷ Various relaxation mechanisms including quantum tunnelling are prevalent to allow the magnetization to be lost.⁸

The evidence of SMM behaviour in a molecular Tb(III) complex, where the Tb(III) is sandwiched by two phthalocyanine ligands, was first reported by Ishikawa and co-workers.⁹ One of the intrinsic features of the lanthanide elements is that the 4f electrons are deeply buried inside the [Xe] core and are considerably shielded by the 5s and 5p electrons. This results in an almost unquenched orbital angular momentum (L) which couples with the spin angular momentum (S) giving rise to the total angular momentum, J .^{4d, 10} Unlike transition metal ions, the magnitude of spin-orbit coupling in the case of 4f metal ions is comparatively much larger than the crystal field and which splits the ground $^{2S+1}L_J$ term into different J multiplets. Although the crystal field effects are small, it has a significant impact on removing the degeneracy of the $(2J + 1) m_j$ microstates corresponding to each of the J multiplets. Since the dynamics of magnetization relies on the relative energies of the ground J manifold, therefore, a suitable crystal field renders the requirement of large splitting between the energy levels giving rise to high energy barrier for magnetization reversal.¹¹

Soon after this discovery, many mononuclear Ln(III) complexes were reported to be SMMs with high energy barriers (U_{eff}) and high blocking temperatures (T_{B}).¹² Among various types of lanthanide complexes, the mononuclear complexes are of considerable interest as they provide a very good understanding of the influence of the ligand field on the observed magnetic properties. The recent reports on mononuclear Dy(III) complexes $[\text{Dy}(\text{Cp}^{\text{tnt}})_2]^+$ ($\text{Cp}^{\text{tnt}} = \text{C}_5\text{H}_2^{\text{t}}\text{Bu}_{3-1,2,4}$) and $[\text{Dy}(\text{Cp}^{\text{iPr5}})(\text{Cp}^*)]^+$ ($\text{Cp}^{\text{iPr5}} = \text{penta-iso-propylcyclopentadienyl}$, $\text{Cp}^* = \text{pentamethylcyclopentadienyl}$) revealing the highest magnetization blocking temperatures of 60 K and 80 K respectively has further spurred activity in this area of mononuclear Ln(III) complexes.¹³

Although ligand fields are much smaller compared to spin-orbit coupling among lanthanide complexes, ironically the former happens to be the most decisive in controlling the performance of SMMs/SIMs. The spatial distribution of the electrons in the different 4f orbitals leads to inherent anisotropic shapes in the Ln(III) ions (except Gd, Eu, La, and Lu). Based on an electrostatic argument, Rinehart and Long have proposed a qualitative model that assists in the designing of SMMs/SIMs.¹⁴ According to this model, an axial ligand field stabilizes the oblate-shaped Ln(III) ions while a prolate-shaped Ln(III) ion requires an equatorial ligand field because such a ligand field minimizes the electrostatic repulsion between the ligands and the metal center and maximizes the molecular magnetic anisotropy. Using this clue a large number of monometallic Ln(III) complexes were prepared with interesting magnetic properties.¹⁵ Among them, the *pseudo*-linear pentagonal bipyramidal complexes in the DyO7, DyClO6, DyXN4O2 (X = Cl and Br), and DyN5O2 coordination environment with strong axial ligand field and weak equatorial ligand field stand out as the most effective systems for the observation of high energy barriers of magnetization reversal.¹⁶

We have been utilizing various types of multidentate ligands for the synthesis of mononuclear Ln(III) complexes. In our previous work, we have synthesized mononuclear pentagonal bipyramidal Ln(III) complexes by employing a pentadentate chelating ligand that provides a rigid equatorial plane.¹⁷ The axial sites in these complexes were occupied by the chloride ions which are considerably weak field ligands compared to N and O donors present in the ligand backbone. We have thoroughly studied the magnetic properties of the Dy(III), Tb(III) and the diluted Dy(III) (in an isostructural Y(III) host) complexes which reveal the molecular origin of slow magnetic relaxation in the Dy(III) derivative with an energy barrier of magnetization reversal of 70 K.¹⁷ To understand the role of the axial ligands in this system we have now prepared a series of neutral mononuclear PBP complexes, [(L)Ln^{III}(R₃PO)Cl] [(Ln = Gd (**1**), Tb (**2**), Dy (**3**), Er (**5**); R = cyclohexyl) and (Ln = Dy (**4**); R = phenyl)] where one phosphine oxide ligand replaces one of the two chloride ligands in the axial sites. Herein, we report the synthesis, structural characterization and magnetic properties of **1-5**. The difference in the magnetic properties has been analyzed by *ab initio* CASSCF/RASSI-SO/SINGLE_ANISO calculation which provides the insight to design the potential SIM.

Experimental Section

Materials and methods. All the reagents and solvents used for the syntheses were used as received from commercial sources. The organic ligand 2,6-diacetylpyridine *bis*-benzoylhydrazone (H₂L) was synthesized following a reported procedure.¹⁸ Fourier transform infrared (FT-IR) spectroscopy was performed with a Bruker FT-IR spectrometer. Elemental analyses were performed with a Perkin–Elmer 2400 series II instrument. Powder X-ray diffraction study was performed on finely ground polycrystalline material with Bruker D8 Advance Powder X-ray diffractometer.

Magnetic Measurements. Magnetic measurements for all the samples were carried out with a Quantum Design MPMS 5S SQUID magnetometer in the temperature range 2–300 K. The measurements were performed on polycrystalline samples. The crystalline powders of the complexes were mixed with grease (except for Gd derivative) and put in gelatin capsules. The temperature dependences of the magnetization were measured in an applied field of 1kOe, and the isothermal field dependence of the magnetizations were collected up to 5 T. The molar susceptibility (χ_M) was corrected for sample holder and for the diamagnetic contribution of all the atoms by using Pascal's tables. AC susceptibility data have been collected in zero field and with applied fields in the frequency range 1–1500 Hz.

X-ray crystallographic studies. The single-crystal X-ray diffraction data of **1-5** were collected on a Rigaku Xtal LAB X-ray Diffractometer system equipped with a CCD area detector and operated at 30 W power (50 kV, 0.6 mA) to generate MoK α radiation ($\lambda = 0.71073 \text{ \AA}$) at 120(2) K. Data were integrated using CrysAlis^{Pro} software with a narrow frame algorithm. Data were subsequently corrected for absorption by the program SCALE3 ABSPACK scaling algorithm.^{13a} All the structures were solved by the direct methods in SHELXTL¹⁹ and refined by the full-matrix least-squares method on F^2 (SHELXL-2014)²⁰ using the Olex-2 software.²¹ All the non-hydrogen atoms were refined with anisotropic thermal parameters. All the hydrogen atoms were included in idealized positions, and a riding model was used. All the mean plane analyses and crystallographic figures have been generated using the DIAMOND software (version 3.2k).²² The crystal data and refinement parameters for **1-5** are summarized in Table 1. More details on the crystallographic data are given in the X-ray crystallographic files in the CIF format.

Synthesis

General procedure. The following general protocol was employed for the synthesis of complexes **1-5**.

The organic ligand, H₂L (1 eq.) was suspended in 30 mL of EtOH and cyclohexyl/phenyl phosphine oxide (1 eq.) was added to it. To this white cloudy solution, the respective LnCl₃·6H₂O (1 eq.) salts were added which results in a yellow solution. The reaction mixture was then heated under reflux conditions for 1 h and allowed to cool to room temperature. To this solution 2 eq. of NEt₃ was added and the solution further stirred at room temperature for 10 minutes. The solvent was evaporated to dryness and the resulting yellow precipitate was washed with diethyl ether. The dried yellow precipitate was then dissolved in 10 mL of EtOH and filtered. The filtrate was kept under vapor diffusion with diethyl ether to afford needle-shaped crystals suitable for X-ray crystallography after one week. The stoichiometry of the reactants involved in each reaction, yield of the products, and their characterization data are provided below:

[(L)Gd(Cy₃PO)Cl] (*1*). H₂L (0.040 g, 0.100 mmol), GdCl₃·6H₂O (0.037 g, 0.100 mmol), Cy₃PO (0.030 g, 0.100 mmol), and Et₃N (28 μL, 0.200 mmol) were used. Yield: 0.053 g, 60% (based on Gd). M.P.: >250 °C. IR (KBr v/cm⁻¹): 3439(br), 3062(w), 2929(s), 2852(m), 1632(w), 1587(m), 1552(m), 1503(s), 1446(m), 1411(m), 1371(s), 1324(m), 1297(m), 1258(w), 1197(w), 1169(m), 1148(m), 1103(s), 1069(w), 1040(s), 987(w), 895(m), 854(w), 809(m), 744(m), 716(s), 679(s), 650(w), 534(m). Anal. Calcd for C₄₁H₅₂Cl₁N₅O₃P₁Gd₁ (886.57): C, 55.55; H, 5.91; N, 7.90. Found: C, 55.21; H, 6.36; N, 7.61.

[(L)Tb(Cy₃PO)Cl] (*2*). H₂L (0.040 g, 0.100 mmol), TbCl₃·6H₂O (0.037 g, 0.100 mmol), Cy₃PO (0.030 g, 0.100 mmol), and Et₃N (28 μL, 0.200 mmol) were used. Yield: 0.059 g, 67% (based on Tb). M.P.: >250 °C. IR (KBr v/cm⁻¹): 3441(br), 3064(w), 2927(s), 2854(m), 1634(w), 1587(m), 1552(m), 1505(s), 1446(m), 1409(m), 1368(s), 1326(m), 1299(m), 1256(w), 1197(w), 1169(m), 1148(m), 1105(s), 1067(w), 1040(s), 987(w), 897(m), 856(w), 809(m), 744(m), 714(s), 679(s), 652(w), 532(m). Anal. Calcd for C₄₁H₅₂Cl₁N₅O₃P₁Tb₁ (888.25): C, 55.44; H, 5.90; N, 7.88. Found: C, 55.02; H, 6.56; N, 7.75.

[(L)Dy(Cy₃PO)Cl] (**3**). H₂L (0.040 g, 0.100 mmol), DyCl₃·6H₂O (0.038 g, 0.100 mmol), Cy₃PO (0.030 g, 0.100 mmol), and Et₃N (28 μL, 0.200 mmol) were used. Yield: 0.061 g, 69% (based on Dy). M.P.: >250 °C. IR (KBr v/cm⁻¹): 3443(br), 3064(w), 2929(s), 2852(m), 1630(w), 1587(m), 1554(m), 1505(s), 1446(m), 1411(m), 1368(s), 1326(m), 1299(m), 1258(w), 1197(w), 1171(m), 1150(m), 1105(s), 1067(w), 1042(s), 989(w), 897(m), 854(w), 809(m), 744(m), 714(s), 679(s), 650(w), 532(m). Anal. Calcd for C₄₁H₅₂Cl₁N₅O₃P₁Dy₁ (891.82): C, 55.22; H, 5.88; N, 7.85. Found: C, 54.85; H, 6.39; N, 7.71.

[(L)Y_{0.90}Dy_{0.10}(Cy₃PO)Cl] (**3'**): Anal. Calcd for C₄₁H₅₂Cl₁N₅O₃P₁Y_{0.90}Dy_{0.10}: C, 60.19; H, 6.41; N, 8.56. Found: C, 59.91; H, 6.52; N, 8.39.

[(L)Dy(Ph₃PO)Cl] (**4**). H₂L (0.040 g, 0.100 mmol), DyCl₃·6H₂O (0.038 g, 0.100 mmol), Ph₃PO (0.028 g, 0.100 mmol), and Et₃N (28 μL, 0.200 mmol) were used. Yield: 0.064 g, 72% (based on Dy). M.P.: >250 °C. IR (KBr v/cm⁻¹): 3429(br), 3054(w), 2919(s), 1632(w), 1587(m), 1552(m), 1499(m), 1438(m), 1409(), 1366(s), 1325(m), 1297(m), 1258(w), 1160(w), 1122(m), 1093(m), 1067(s), 1044(w), 989(w), 897(m), 809(m), 744(m), 714(s), 691(), 650(2), 540(m). Anal. Calcd for C₄₁H₃₄Cl₁N₅O₃P₁Dy₁ (873.68): C, 56.37; H, 3.92; N, 8.02. Found: C, 55.98; H, 3.61; N, 7.89

[(L)Er(Cy₃PO)Cl] (**5**). H₂L (0.040 g, 0.100 mmol), ErCl₃·6H₂O (0.038 g, 0.100 mmol), Cy₃PO (0.030 g, 0.100 mmol), and Et₃N (28 μL, 0.200 mmol) were used. Yield: 0.065 g, 73% (based on Er). M.P.: >250 IR (KBr v/cm⁻¹): 3447(br), 3068(w), 2929(s), 2852(m), 1636(w), 1587(m), 1554(m), 1505(s), 1446(m), 1413(m), 1366(s), 1326(m), 1299(m), 1260(w), 1199(w), 1169(m), 1152(m), 1107(s), 1067(w), 1044(s), 989(w), 897(m), 854(w), 809(m), 746(m), 714(s), 679(s), 650(w), 534(m). Anal. Calcd for C₄₁H₅₂Cl₁N₅O₃P₁Er₁ (896.58): C, 54.93; H, 5.85; N, 7.78. Found: C, 54.65; H, 6.33; N, 7.53.

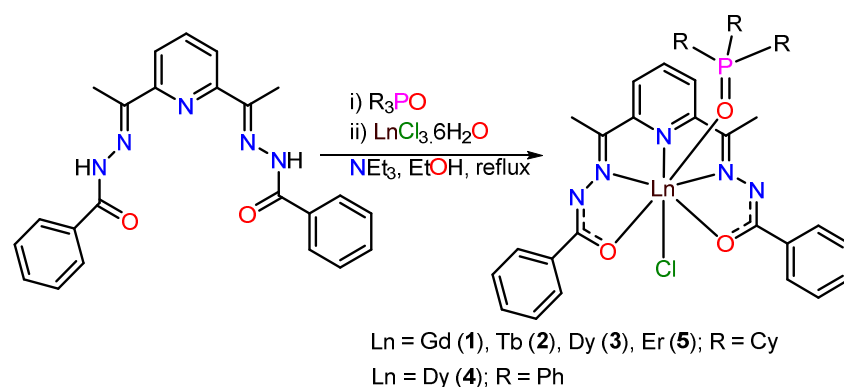
Computational Details

Post-Hartree-Fock *ab initio* calculations were carried out on the X-ray crystal structures of all complexes using the CASSCF+RASSI-SO+SINGLE_ANISO approach as implemented in MOLCAS 8.2 programme package.²³ The relativistic effects of the lanthanide ions have been incorporated using the DKH Hamiltonian.²⁴ The basis set of all the atoms (Table S8 in ESI) has been taken from the ANO-RCC library implemented in MOLCAS 8.2 suite. First, we have performed CASSCF calculations by considering 8, 9 and 11 electrons in the seven 4f orbitals of Tb(III), Dy(III) and Er(III) ions in their respective complexes. Using this active space, we have computed 7 septet, 140 quintet and 195 triplet states for Tb(III), 21 sextet states for Dy(III), 35 quartet and 112 doublet states for Er(III) ion. These spin free states of each complex were mixed by RASSI-SO to calculate the spin-orbit energy levels. Finally, the g tensors and mechanism of magnetization relaxations were estimated using the SINGLE_ANISO which interfaced with the RASSI-SO energies. In a nutshell, CASSCF/RASSI-SO/SINGLE_ANISO method was used to compute the magnetic anisotropy, energy of the spin free and spin-orbit states and the magnetic relaxation dynamics.

Results and Discussion

Synthetic aspects. The PBP geometry is regarded as one of the most promising coordination geometries around the Ln(III) center that can bring axiality in the ground state of Ln(III) ions provided the axial sites are occupied by comparatively strong donor ligands. We have previously reported the synthesis of mononuclear pentagonal bipyramidal Ln(III) complexes using a pentadentate chelating ligand which effectively provides a rigid equatorial plane. In these complexes, the two axial sites were occupied by chloride ions which can be regarded as weak field ligands compared to the N and O donor atoms of the pentadentate chelating

ligand. Theoretical studies accompanied by experimental evidence show that oblate shaped Ln(III) ions show high energy barriers of magnetization in the PBP geometry when the axial sites are occupied by relatively strong donor ligands compared to the equatorial sites. Keep this in mind we have chosen tri-alkyl/aryl phosphine oxides to replace the chloride ions in the axial sites. Accordingly, when we treated the ligand H₂L with lanthanide chlorides in the presence of phosphine oxides followed by addition of base we obtained neutral mononuclear [(L)Ln^{III}(R₃PO)Cl] (Ln = Dy Tb, Gd, Er when R = cyclohexyl; Ln = Dy when R = phenyl) complexes (Scheme 1).



Scheme 1. Reaction scheme for the synthesis of **1–5**.

X-ray Crystallography

The complexes **1**, **3** and **5** crystallize in the monoclinic crystal system with *P2₁/c* (for **3**) and *P2₁/n* (for **1** and **5**) space groups whereas the complexes **2** and **4** crystallize in the triclinic crystal system with *P-1* space group. Crystallographic data and refinement parameters of all the complexes are given in Table S1. The overall molecular structures of the complexes **1–5** are essentially identical. The molecular structure of complex **3** is shown in Figure 1, while those of **1**, **2**, **4** and **5** are given in the Supporting Information (Figures S1-S4). In view of the structural similarities present in the complexes we discuss below the molecular structures of complexes **3** and **4**.

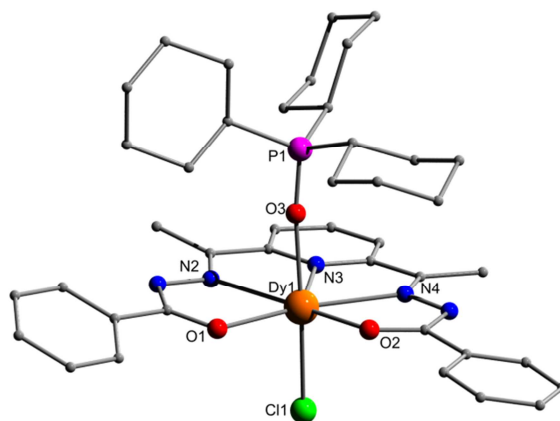


Figure 1. Molecular structure of complex **3**. (The H atoms are removed for clarity)

The complexes are formed by the coordination action of ligand *pyridyl* N atom, two *imino* N atoms, and two *carboxy* O atoms in the equatorial positions. One of the two axial sites is occupied by one chloride anion in both the two complexes. The remaining axial site is occupied by one C_3PO ligand in the case of **3** and Ph_3PO ligand in the case of **4**. The ligand upon chelation with the Ln(III) ions generates four *five*-membered rings revealing its excellent ability to stabilize the Ln(III) ions in its pentagonal coordination environment. The equatorial Dy–O/N bond distances are in the range of 2.259(2)–2.462(2) Å for **3** and 2.282(2)–2.456(2) Å for **4**. The Dy–O_{axial} bond distances are 2.237(2) for **3** and 2.275(2) for **4**. The Dy–Cl bond distances are 2.625(8) Å for **3** and 2.622 (7) Å for **4**. Interestingly, the Dy–O_{axial} bond distance in both **3** and **4** are shorter compared to the Dy–O_{equatorial} distances (Table S2 and Table S4) indicating the strong-field nature of the phosphine oxide ligand in comparison to the equatorial oxygen donors. The O_{phos}–Dy–Cl bond angles are 169.62(5)° for **3** and 174.07(5)° for **4**. The immediate coordination environment the Ln(III) ions are analyzed with Continuous-Shape Measures using the SHAPE program.²⁵ It reveals a distorted pentagonal bipyramid geometry around the Dy(III) ions with D_{5h} (*pseudo*) CF symmetry (Table S3, see ESI). The pentagonal bipyramidal geometry of the Dy(III) ion in complex **3** is shown in Figure 2 (*left*). The shortest intermolecular

Ln····Ln distance in **1**, **3** and **4** is 8.47 Å, 8.56 Å, and 8.80 Å respectively as revealed in the solid-state packing diagram (see Figure 2 (*right*) for complex **3** and Figures S5 and S6 for **1** and **4**). The solid state phase purity of the complex **3'** was confirmed by powder X-ray diffraction studies (Figure S7 see ESI). The selected bond lengths and bond angles of complexes **1**, **2**, **4** and **5** are summarized in Table S4 (see ESI).

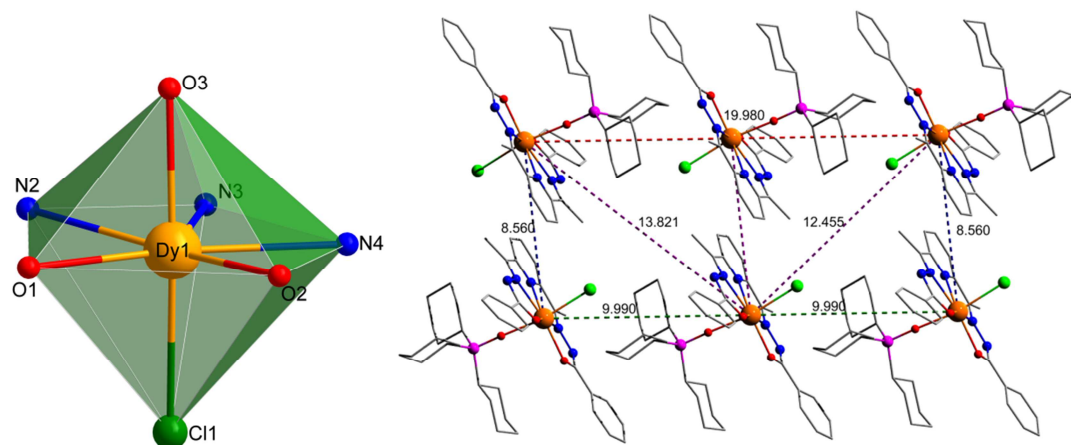


Figure 2. (*left*) Coordination polyhedra of Dy(III) and (*right*) solid-state packing diagram of complex **3**.

Magnetic Properties

The temperature dependence of the molar magnetic susceptibility (χ_M) for **1-3** and **5** are plotted in Figure 3 and the field dependence of the magnetization for these compounds can be found in Figure S9. The corresponding behavior for **4** is summarized in Figure S8. The values of the product of the molar magnetic susceptibility with temperature, $\chi_M T$ (in $\text{cm}^3 \text{mol}^{-1} \text{K}$) found at 300 K are 7.85 (Gd), 11.79 (Tb), 14.14 and 14.10 (Dy), and 11.18 (Er), in good accordance with the expected values expected for the isolated ions (i.e. 7.88, 11.81, 14.17, and 11.48 $\text{cm}^3 \text{mol}^{-1} \text{K}$, respectively). For the Tb, Dy, and Er derivatives the $\chi_M T$ slowly decreases as T is lowered in agreement with the anticipated crystal field effect. The absence of any contribution from intermolecular exchange interactions is confirmed by the perfect Curie behavior down to 2 K for Gd. For the Tb and Dy derivatives, the field-dependent

magnetization at 2-5 K show a fast rise at lower field regions and remain almost unchanged above 15 kOe (at 2 K) to reach 4.8 μB (2), 5.14 (3), and 5.09 (4) at high field (5 T). To probe the dynamics of the magnetization relaxation, AC susceptibility behavior was investigated without and with applied static fields. No out-of-phase component (χ''_{M}) were found for the Tb and Er derivatives down to 2 K (see Figure S10 in ESI). However, the Dy complexes **3** and **4** exhibited a χ''_{M} signal but no maximum was observed above 2 K (see Figure S10 in ESI).

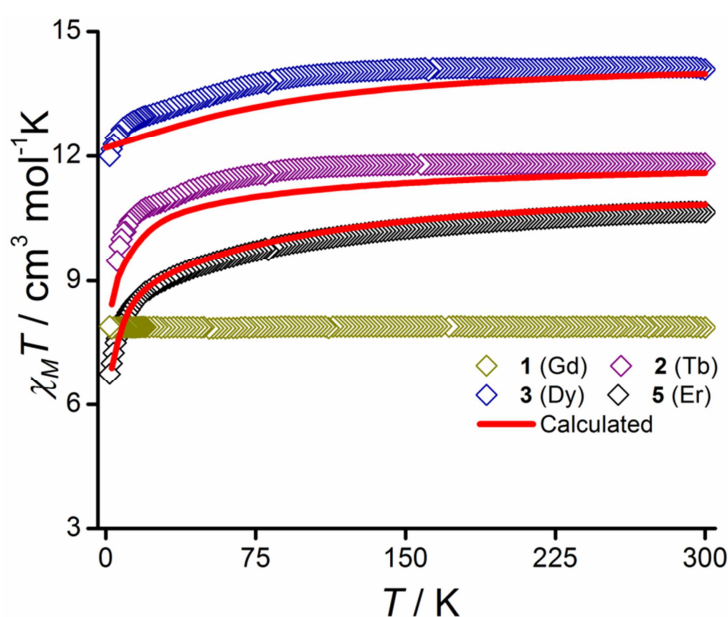
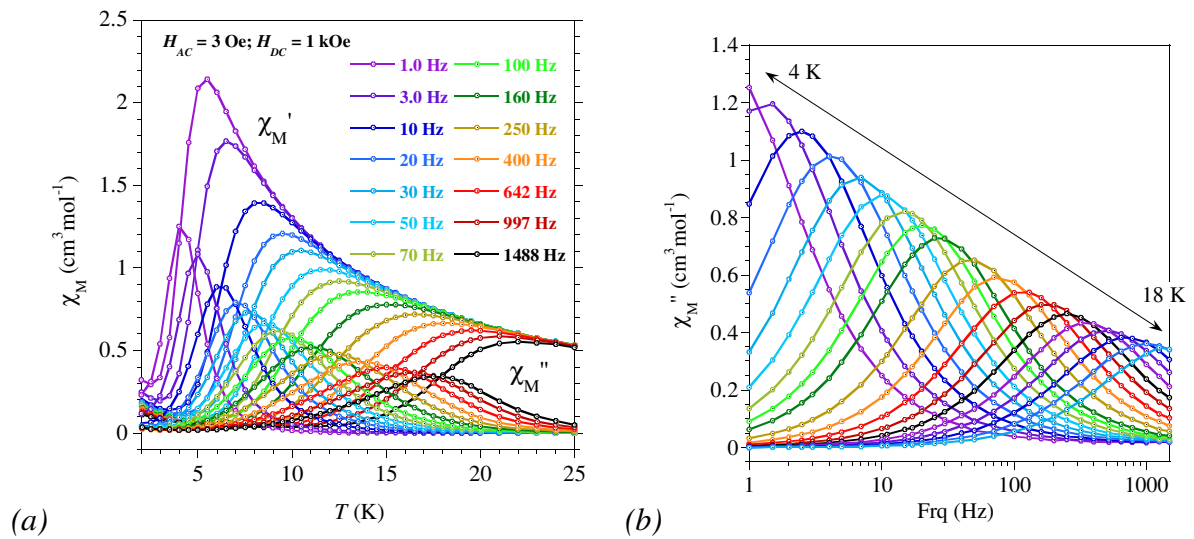


Figure 3. Temperature dependence of the product of the molar magnetic susceptibility with temperature, $\chi_{\text{M}}T$, under 1 kOe applied magnetic field for complexes **1-3** and **5**. Solid red lines represent the *ab initio* calculated data. The computed data for **5** was reduced by 2% to meet the experimentally observed.

Such a behaviour was suggesting relaxation driven by QTM which was reduced by applying a static field. For **3**, the optimum applied field was estimated at $H_{\text{DC}} = 1$ kOe (See Figure S11). AC susceptibility study carried out in this field within the frequency domain 1–1500 Hz yielded well-defined maxima for χ''_{M} between 4 and 18 K (Figure 4). Relaxation times (τ)

have been assessed by fitting $\chi''_M = f(\text{Frq})$ for different temperatures with an extended Debye model, best fit parameters are gathered in Table S5. The very small a parameter is indicative for a narrow distribution width for the relaxation time over the whole temperature domain, suggesting that mainly one relaxation process is operative. The temperature dependence of the relaxation time, plotted in log scale in Figure 4, develops to a more linear variation above 10 K, which is the behavior anticipated for a thermally activated process (Orbach). Deviation from linearity for lower T indicates that other processes also come into play. Analysis of the behavior over the whole T range was obtained by summing the contributions of the Orbach, Raman, and direct processes ($\tau = \tau_0 \exp(U_{\text{eff}}/k_B T) + 1/(CT^n) + 1/(AT)$). The latter were required to reproduce the lower T behavior. Best fit gave a thermal energy barrier for magnetization reversal, $U_{\text{eff}}/k_B = 204 \pm 3$ K with $\tau_0 = (6 \pm 1) \times 10^{-9}$ s, $C = 0.015 \text{ K}^{-1} \text{ s}^{-1}$, $n = 4.5$, and $A = -1.30 \text{ s}^{-1}$.



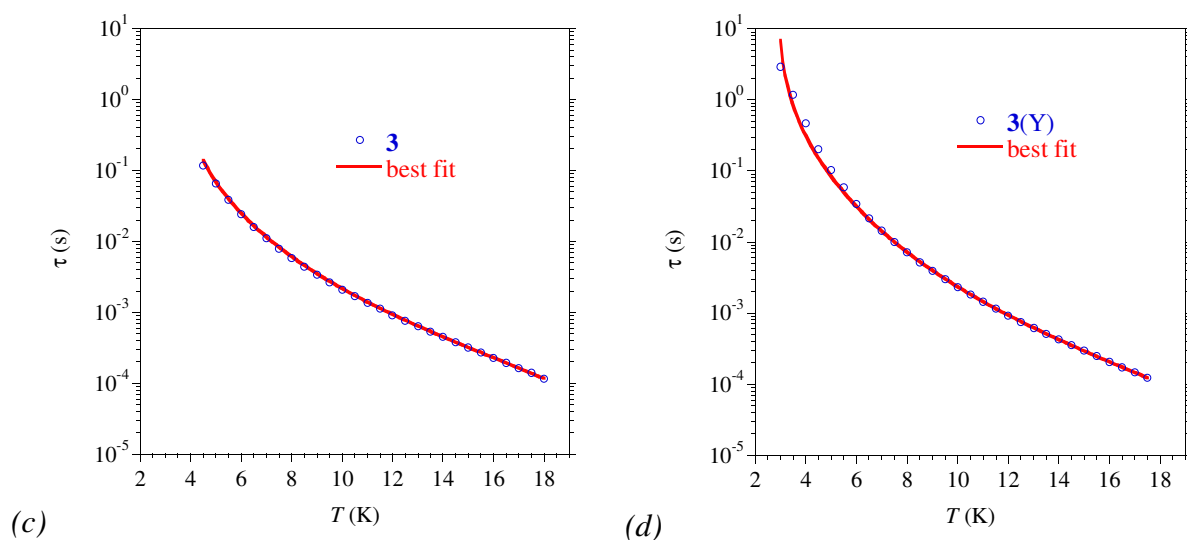


Figure 4. (a,b) AC susceptibility behaviors for **3**; (c) temperature dependence of the relaxation times for **3**, and (d) for diluted compound **3'**; the solid red lines are the best fits (see text).

The dilution of **3** in a matrix of isomorphous Y complex, **3'** hereafter, gave very similar results (see Figure S12 in ESI). For this sample however, a maximum was observed in the $\chi''_{\text{M}} = f(T)$ behavior in zero field but a QTM contribution was discernible at low temperature. This was suppressed upon applying a small DC field of 750 Oe. The temperature dependence of the relation times between 2 and 17.5 K (Figure 4 and Table S6) parallels that obtained for the pure Dy derivative **3**, and contributions of the Orbach, Raman, and direct processes had to be taken into account to reach a good modeling. Best fit to the experimental data for **3'** yielded $U_{\text{eff}}/k_{\text{B}} = 208 \pm 5$ K, $\tau_0 = (6 \pm 2) \times 10^{-9}$ s, $C = 4.3 \times 10^{-3} \text{ K}^{-1} \text{ s}^{-1}$, $n = 5.0$, and $A = -0.30 \text{ s}^{-1}$. The comparison of the behavior for **3** and its diluted form **3'** shows that the observed behavior is clearly of molecular origin.

The replacement of OPCy_3 for OPPh_3 in the apical position of Dy appeared to have no significant incidence on the magnetic behaviours; the AC susceptibility features for **4** (Figure

S13 and Table S7 in ESI) are very similar to that obtained for **3**. To reproduce the temperature dependence of the relaxation time for **4** required to consider contributions from Orbach, Raman and direct processes, best fit to the experimental behavior gave $U_{\text{eff}}/k_B = 241 \pm 7$ K, $\tau_0 = (2.3 \pm 0.9) \times 10^{-10}$ s, $C = (5.97 \pm 0.03) \times 10^{-3} \text{ K}^{-1} \text{ s}^{-1}$, $n = 5.1$, and $A = 0.2 \pm 0.7 \text{ s}^{-1}$.

It is satisfying to see that the energy barrier for magnetization reversal, U_{eff}/k_B , for the Dy(III) complexes reported herein is significantly increased with respect to the homologue complex with Cl^- ligands in the apical positions. This could be attributed to the stronger axial field due to the phosphine oxide ligand. A detailed comparison of the bond and magnetic properties of the present complexes with the reported pentagonal bipyramidal Dy(III) complexes having other equatorial ligands (including monodentate ones) and axial groups of various crystal field strengths are given in Table 1.

Table 1. Selected bond and magnetic parameters of PBP Dy(III) complexes

Sl. No.	Complex	$L_{\text{ax}}-\text{Ln}-L_{\text{ax}}$ ($^\circ$)	Average axial Ln-O/Ln-X distance (\AA)	Average equatorial Ln-O/Ln-N/Ln-X distance (\AA)	U_{eff} (K) (H_{dc})	τ_0 (s)	Ref.
1	$[\text{Dy}(\text{O}^t\text{Bu})_2(\text{py})_5][\text{BPh}_4]$	155.80	2.112	2.557	1815 (0 Oe)	1.17×10^{-12}	[^{16c}]
2	$[\text{Dy}(\text{bbpen})\text{Br}]$	155.79	2.163	2.586/2.851	1025 (0 Oe)	4.21×10^{-12}	[^{16c}]
3	$[\text{Dy}(^t\text{BuO})\text{Cl}(\text{THF})_5][\text{BPh}_4] \cdot 2\text{THF}$	178.28	2.043/2.662	2.410	950 (0 Oe)	3×10^{-12}	[²⁶]
4	$[\text{Dy}(\text{bbpen})\text{Cl}]$	154.24	2.166	2.584/2.682	708 (0 Oe)	9.46×10^{-11}	[^{16c}]
5	$[\text{L}_2\text{Dy}(\text{H}_2\text{O})_5][\text{I}]_3 \cdot (\text{L}^1)_2 \cdot \text{H}_2\text{O}$	177.9	2.205	2.363	651 (0 Oe)	5.63×10^{-12}	[^{16b}]
6	$[\text{Dy}(\text{L}^2)_2(\text{H}_2\text{O})_5]_2 \cdot \text{Br}_6 \cdot 2\text{L}^2 \cdot 2\text{H}_2\text{O}$	177.82	2.221	2.354	556 (0 Oe)	9.33×10^{-12}	[²⁷]
7	$[\text{Dy}(\text{Cy}_3\text{PO})_2(\text{H}_2\text{O})_5]\text{Br}_3 \cdot 2(\text{Cy}_3\text{PO}) \cdot 2\text{H}_2\text{O} \cdot 2\text{EtOH}$	179.04	2.200	2.352	543 (0 Oe)	2.0×10^{-11}	[²⁸]

8	[Dy(CyPh ₂ PO) ₂ (H ₂ O) ₅] Br ₃ ·2(CyPh ₂ PO)·EtOH· 3H ₂ O	174.2	2.217	2.364	508 (0 Oe)	8.6 × 10 ⁻¹²	[²⁹]
9	[Dy(Cy ₃ PO) ₂ (H ₂ O) ₅]Cl ₃ · (Cy ₃ PO)·H ₂ O·EtOH	175.79	2.219	2.359	472 (0 Oe)	8.7 × 10 ⁻¹²	[²⁸]
10	[(NCN)DyCl ₂ (THF) ₂]	176.50	2.596	2.448/2.668 2.393 (Dy–C)	335 (0 Oe)	6 × 10 ⁻¹⁰	[³⁰]
11	[DyCl ₂ (THF) ₅][BPh ₄]	179.68	2.577	2.390	80.6 (0 Oe)	4.1 × 10 ⁻¹⁰	[³¹]
12	[Dy(Bpen)Cl(OPhCl ₂ NO 2) ₂]	165.60	2.174	2.523/2.616	86 (1 kOe)	4.65 × 10 ⁻⁷	[³²]
13	[(H ₂ L ³)Y _{0.94} Dy _{0.06} Cl ₂]	166.32	5.643	2.264/2.444	70 (0.5 kOe)	1.9 × 10 ⁻⁶	[¹⁷]
14	[(L ⁴)Dy(Cy ₃ PO)Cl]	169.62	2.237/2.625	2.265/2.458	204 (1 kOe)	6.0 × 10 ⁻⁹	This work
15	[(L ⁴)Dy(Ph ₃ PO)Cl]	174.07	2.276/2.623	2.283/2.460	241 (1.5 kOe)	2.3 × 10 ⁻¹⁰	This work

L¹ = (tBuPO(NHⁱPr)₂); L²: hexamethylphosphoric triamide; H₂bbpen = *N,N'*-bis(2-hydroxybenzyl)-*N,N'*-bis(2-methylpyridyl)ethylenediamine); NCN: [2,6-(2,6-C₆H₃R₂N₅CH)₂C₆H₃]⁻; Bpen: *N,N'*-bis(2-methylenepyridinyl)ethylenediamine; H₄L³: 2,6-diacetylpyridine bis-salicylhydrazone; H₂L⁴: 2,6-diacetylpyridine bis-benzoylhydrazone

Computational study

In order to rationalize the experimentally observed magnetization relaxation, we have performed *ab initio* CASSCF/RASSI+SO/SINGLE_ANISO calculations²³ on the X-ray structures of complexes **2-5** and the previously reported complex **6**¹⁷ in which both the axial positions were occupied by the Cl⁻ ligands. The X-ray analysis revealed that complexes **2** and **5** consist of two molecules in the asymmetric unit and we have performed our calculations on the one molecule for each of the complexes.

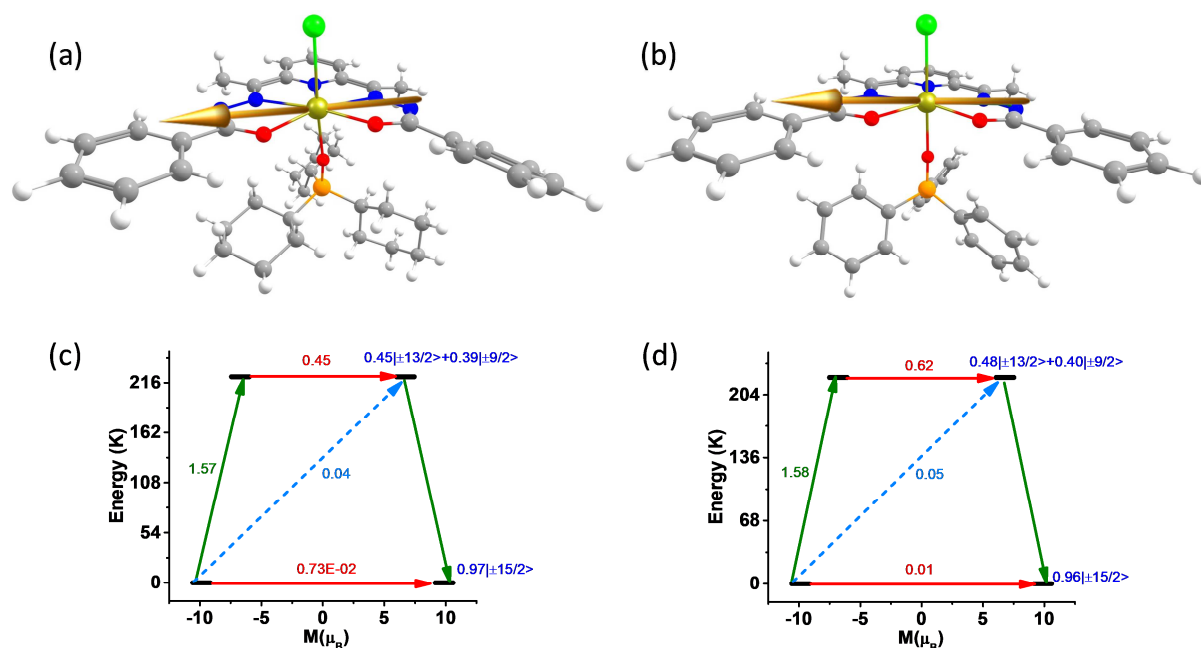


Figure 5. Orientation of the anisotropy axis of Dy(III) ion in complex **3** (a) and **4** (b). (c) and (d) represent the plausible relaxation mechanism for **3** and **4** respectively. The red arrows show the QTM and TA-QTM via ground and higher excited KD respectively. The sky dotted arrows show the Orbach process for the relaxation. The green arrows show the possible mechanism of magnetic relaxation. The blue characters imply the m_j composition of the KDs.

Table 2. The computed energy and the associated g-tensors of the low lying KDs generated from ${}^6\text{H}_{15/2}$ state of complexes **3**, **4** and **6**.

Energy (K)	g_x	g_y	g_z	The angle of g_{zz} axis between the ground and higher excited KDs ($^\circ$)
Complex 3				
0.0	0.013	0.030	19.741	
222.6	0.910	1.684	13.977	16.2
277.1	0.661	3.360	11.281	19.3
334.9	0.044	1.050	13.447	87.8
516.4	1.005	3.829	12.313	3.6
599.6	2.148	5.995	13.311	92.5
700.0	0.467	1.645	12.249	90.7
903.6	0.145	0.743	17.531	90.4
Complex 4				
0.0	0.020	0.041	19.734	
222.9	0.954	2.781	13.614	3.7
284.1	0.627	1.875	11.962	6.0

398.2	1.326	1.612	16.936	88.6
518.3	0.969	4.094	12.524	16.4
624.5	11.040	6.990	1.617	89.9
724.2	1.384	3.050	11.564	91.1
903.2	0.108	0.870	17.209	90.1
Complex 6				
0.0	0.009	0.016	19.741	
211.0	0.454	1.287	14.174	0.0
281.1	0.683	0.816	12.236	0.0
509.2	1.955	3.683	11.188	90.0
635.5	0.010	2.340	16.111	90.0
704.3	1.061	3.553	10.520	90.0
829.9	3.445	5.293	8.380	90.0
942.3	1.253	1.728	15.285	90.0

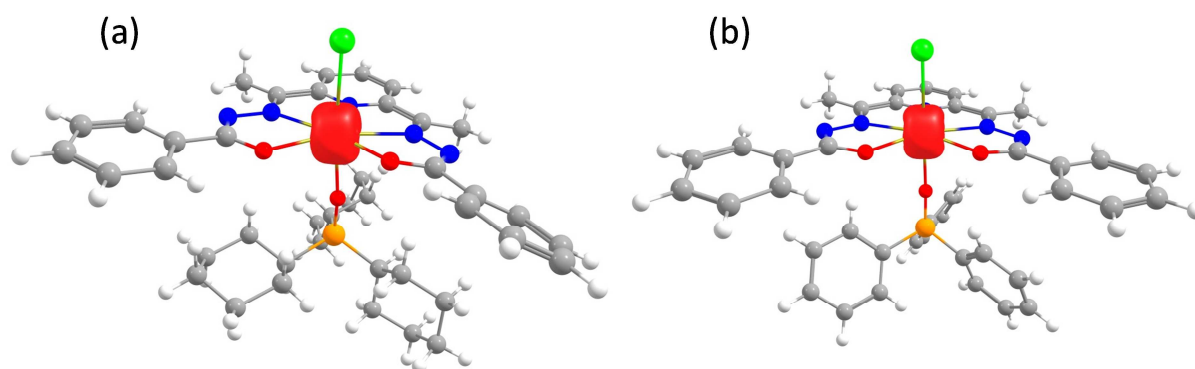


Figure 6. (a) The beta electron density of complex **3**. (b) The beta electron density of complex **4**. Colour code: Dy-yellow, Cl-green, P-violet, O-red, N-blue, C-grey, H-white.

The computed energy of the eight low lying KDs generated from ${}^6\text{H}_{15/2}$ state spans from zero to 903 K in complexes **3** and **4** and 942 K in complex **6** (Table 2). The g tensors; $g_x \approx g_y \approx 0$ and $g_z \approx 20$ for complexes **3**, **4** and **6** demonstrate the *Ising* behavior of Dy(III) ion in these complexes. The g_{zz} axis of ground KD is found to be lying on the equatorial plane due to the strong crystal field generated from the equatorial ligand (Figure 5 and S14). We have plotted the beta electron density of Dy in complexes **3**, **4** and **6** using the procedure introduced by Ruiz and coworkers.³³ Since the beta electron density is found to orient along the axial Cl–Dy–O bond (Cl–Dy–Cl bond in **6**), the g_{zz} anisotropy axis is oriented along the perpendicular direction of it to minimize the electrostatic repulsion (Figure 6). The large thermally assisted

quantum tunneling (TA-QTM) value of 0.41, 0.64 and 0.24 μ_B in the first excited KDs suggest the relaxation will occur ideally through the first excited state KD (Figure 5 and S14). This suggests U_{cal} value of 222.6, 222.9 and 211.0 K for complexes **3**, **4** and **6** respectively. These values are consistent with the estimate obtained from the experiments except for **6** where U_{cal} values are overestimated (for **3** 208 K, **4** 241 K and **6** 70 K). We have also analyzed the composition of the computed wave function to get more insight about the extent of mixing of the m_J levels. The ground KD is found to be consist of $m_J = \pm 15/2$ ($\approx 97\%$) with the negligible ($\approx 0.02\%$) mixing with $m_J = \pm 11/2$ states. The strong mixing in the first excited KD leads to very large TA-QTM which forces the complex to relax via this state.

The *ab initio* computed energy barrier for the magnetization reversal does not affect significantly when one Cl^- ion in the axial position (complex **6**) is replaced by the neutral Cy_3PO or Ph_3PO ligand (complexes **3** and **4** respectively). The energy spectrum depends on the ligand field generated from the equatorial ligands which is found to be same in all the complexes. We have analyzed the LoProp charges to get more insight into the axiality of the three complexes. The LoProp charge of the axial oxygen atoms is found to be larger than the equatorial nitrogen and oxygen atoms in **3** and **4** (Table S9 and Figure S15). More importantly, the ratio of the av. axial/equatorial LoProp charges is found to be almost same in the complexes **3** and **4** which is consistent with similar U_{cal} values estimated in these complexes. The LoProp charge of the axial chlorine atoms and equatorial oxygen atoms is found to be very close in **6** which imply the less axial nature of this complex compared to **3** and **4**. However the av. axial/equatorial LoProp charge >1.7 implies significant axiality in this complex.

The crystal field parameter of the three complexes has been estimated using the Steven formalism ($\hat{H}_{CF} = \sum \sum_{k=-q}^{+q} B_k^q \tilde{O}_k^q$, where B_k^q and \tilde{O}_k^q is computed crystal field parameter and

Stevens operator respectively) as implemented in SINGLE_ANISO suite to get more insight on the relaxation mechanism. The axial crystal field parameter B_2^0 is found to be larger in **4** compare to **3** implies the stronger axially in **4** which agrees well with the U_{eff} value (Table S10). However the B_2^2 value in complex **6** is found to be similar implies lower axially here compare to **3** and **4**.

Furthermore, we have modeled the complex **3a**, **4a** and **6a** (where the equatorial ligand has been removed) from complexes **3**, **4** and **6** respectively to achieve the axial limit in each of these complexes. The anisotropy axis is found to be oriented along the Cl–Dy–O bond due to the absence of equatorial ligand field (Figure S16). The beta electron density is found to be oblate in nature and the g_{zz} axis is oriented along the axial Cl–Dy–O bond (Cl–Dy–Cl bond in **6**) to minimize the electrostatic repulsion (Figure 7). The *ab initio* calculations on these models reveal that the energy splitting of the eight KDs generated from ${}^6\text{H}_{15/2}$ state raises to 2864, 2787 and 2616 K for **3a**, **4a** and **6a** respectively (Table S11). Absence of equatorial ligand field leads to higher LoProp charge in the Dy center and metal coordinated oxygen atoms revealing the axial limit that can be achieved in these set of complexes (Table S12). It is also reflected in the computed crystal field parameter in which larger B_2^0 value is found compare to original complexes (Table S13). The magnetization relaxation is found to occur via fourth excited KD due to the strong transverse anisotropy which leads to U_{cal} value of 2540, 2471 and 2248 K in **3a**, **4a** and **6a** respectively (Figure S17).

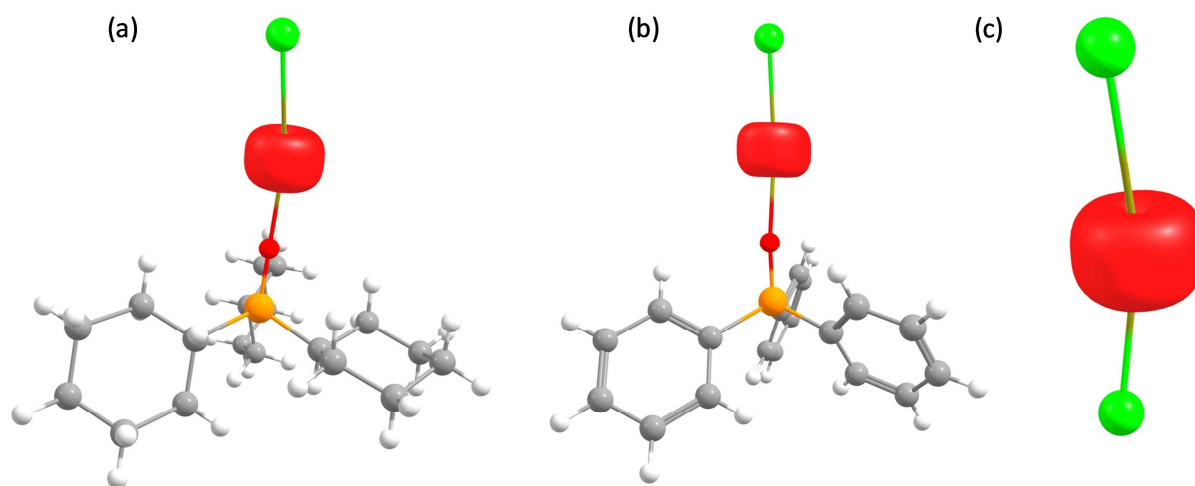


Figure 7. (a) The beta electron (spin-down) density of model **3a**. (b) The beta electron density of model **4a**. (c) The beta electron density of model **6a**. Colour code: Dy-yellow, Cl-green, P-violet, O-red, N-blue, C-grey, H-white.

In the case of complex **2**, a large tunnel splitting (Δ_{tun}) of 2.26 cm^{-1} is found between the two pseudo ground KDs which triggers the magnetization relaxation via the ground state (Table S14). The ground state anisotropy axis is found to be lying on the equatorial plane due to the strong equatorial ligand field (Figure S18). In case of complex **5** the computed large QTM value of $0.22 \mu_B$ between the ground state KD also suggests the relaxation via ground state which is supported by no out-of-phase signals in ac susceptibility (Figure S18 and Table S15).

Summary

Mononuclear 4f complexes (Gd^{III} , Dy^{III} , Er^{III} and Tb^{III}) have been assembled using a multifunctional chelating ligand. The ligand enforces a pentagonal equatorial architecture around the metal ion. The two axial sites are taken up by a chloride and a phosphine oxide ligand. Thus, the overall coordination geometry around the lanthanide metal ion is distorted pentagonal bipyramidal. Magnetic studies on these complexes reveal that the Dy^{III} analogues

show a slow relaxation of magnetization under the presence of small DC fields. A large tunneling gap between the ground as well as consequent excited non-Kramers doublets of Tb^{III} and a very high quantum tunneling between the ground state Kramers doublets in the Er^{III} complex prevents these complexes from revealing a single-ion magnet behavior. The strategy adopted in the present instance of using a rigid ligand that enforces a pentagonal equatorial plane around the lanthanide ion is clearly effective in enabling the designed assembly of single-ion magnets. An improvement in this strategy would be to effect modifications in the ligand design to decrease the effective crystal field in the equatorial plane and increase it in the axial sites. We are currently examining these possibilities.

Acknowledgements

V. C. is thankful to the Department of Science and Technology, New Delhi, India, for a National J. C. Bose Fellowship. P. K. is thankful to National Institute of Science Education and Research, Bhubaneswar and Tata Institute of Fundamental Research, Hyderabad for doctoral and post-doctoral fellowships respectively. N.A is thankful to Tata Institute of Fundamental Research, Hyderabad for a post-doctoral fellowship. S. D. thanks UGC for SRF fellowship. GR would like to acknowledge SERB for funding (CRG/2018/000430).

Supporting Information

CCDC 1989266 (1), 1989267(2), 1989268(3), 1989270(4), 1989271(5) contain crystallographic supplementary data for this paper. These data can be obtained free of charge from The Cambridge Crystallographic Data Centre via www.ccdc.cam.ac.uk/data_request/cif.

X-ray crystallographic table of complexes 1–5; molecular structures of complexes 1, 2, 4 and 5; crystal packing diagrams of 1 and 4. table of bond distances and angles; table of continuous shape measures calculations; powder X-ray diffraction pattern of 3'. details of magnetic properties of 1–5; details of computational calculations of complexes 1–5 (PDF).

References

1. (a) Robinson, J. R.; Fan, X.; Yadav, J.; Carroll, P. J.; Wooten, A. J.; Pericàs, M. A.; Schelter, E. J.; Walsh, P. J. Air- and Water-Tolerant Rare Earth Guanidinium BINOLate Complexes as Practical Precatalysts in Multifunctional Asymmetric Catalysis. *J. Am. Chem. Soc.* **2014**, *136*, 8034-8041; (b) Chen, S.; Yan, D.; Xue, M.; Hong, Y.; Yao, Y.; Shen, Q. Tris(cyclopentadienyl)lanthanide Complexes as Catalysts for Hydroboration Reaction toward Aldehydes and Ketones. *Org. Lett.* **2017**, *19*, 3382-3385; (c) Halter, D. P.; Palumbo, C. T.; Ziller, J. W.; Gembicky, M.; Rheingold, A. L.; Evans, W. J.; Meyer, K. Electrocatalytic H₂O Reduction with f-Elements: Mechanistic Insight and Overpotential Tuning in a Series of Lanthanide Complexes. *J. Am. Chem. Soc.* **2018**, *140*, 2587-2594; (d) Nagae, H.; Aoki, R.; Akutagawa, S.-n.; Kleemann, J.; Tagawa, R.; Schindler, T.; Choi, G.; Spaniol, T. P.; Tsurugi, H.; Okuda, J.; Mashima, K. Lanthanide Complexes Supported by a Trizinc Crown Ether as Catalysts for Alternating Copolymerization of Epoxide and CO₂: Telomerization Controlled by Carboxylate Anions. *Angew. Chem. Int. Ed.* **2018**, *57*, 2492-2496; (e) Schmidt, B. M.; Pindwal, A.; Venkatesh, A.; Ellern, A.; Rossini, A. J.; Sadow, A. D. Zwitterionic Trivalent (Alkyl)lanthanide Complexes in Ziegler-Type Butadiene Polymerization. *ACS Catal.* **2019**, *9*, 827-838.
2. (a) Bünzli, J.-C. G. On the design of highly luminescent lanthanide complexes. *Coord. Chem. Rev.* **2015**, *293-294*, 19-47; (b) Hirai, Y.; Nakanishi, T.; Kitagawa, Y.; Fushimi, K.; Seki, T.; Ito, H.; Hasegawa, Y. Luminescent Europium(III) Coordination Zippers Linked with Thiophene-Based Bridges. *Angew. Chem. Int. Ed.* **2016**, *55*, 12059-12062; (c) Wei, H.; Zhao, Z.; Wei, C.; Yu, G.; Liu, Z.; Zhang, B.; Bian, J.; Bian, Z.; Huang, C. Antiphotobleaching: A Type of Structurally Rigid Chromophore Ready for Constructing Highly Luminescent and Highly Photostable Europium Complexes. *Adv. Funct. Mater.* **2016**,

26, 2085-2096; (d) Kovacs, D.; Lu, X.; Mészáros, L. S.; Ott, M.; Andres, J.; Borbas, K. E. Photophysics of Coumarin and Carbostyryl-Sensitized Luminescent Lanthanide Complexes: Implications for Complex Design in Multiplex Detection. *J. Am. Chem. Soc.* **2017**, *139*, 5756-5767; (e) Martinić, I.; Eliseeva, S. V.; Nguyen, T. N.; Pecoraro, V. L.; Petoud, S. Near-Infrared Optical Imaging of Necrotic Cells by Photostable Lanthanide-Based Metallacrowns. *J. Am. Chem. Soc.* **2017**, *139*, 8388-8391; (f) Xiang, S.; Bao, D.-X.; Wang, J.; Li, Y.-C.; Zhao, X.-Q. Luminescent lanthanide coordination compounds with pyridine-2,6-dicarboxylic acid. *J. Lumin.* **2017**, *186*, 273-282; (g) Qiao, Y.; Schelter, E. J. Lanthanide Photocatalysis. *Acc. Chem. Res.* **2018**, *51*, 2926-2936; (h) Du, Y.; Jiang, Y.; Sun, T.; Zhao, J.; Huang, B.; Peng, D.; Wang, F. Mechanically Excited Multicolor Luminescence in Lanthanide Ions. *Adv. Mater.* **2019**, *31*, 1807062.

3. (a) Strnat, K.; Hoffer, G.; Olson, J.; Ostertag, W.; Becker, J. J. A Family of New Cobalt-Base Permanent Magnet Materials. *J. Appl. Phys.* **1967**, *38*, 1001-1002; (b) Vincent, R.; Klyatskaya, S.; Ruben, M.; Wernsdorfer, W.; Balestro, F. Electronic read-out of a single nuclear spin using a molecular spin transistor. *Nature* **2012**, *488*, 357-360; (c) Woodruff, D. N.; Winpenny, R. E. P.; Layfield, R. A. Lanthanide Single-Molecule Magnets. *Chem. Rev.* **2013**, *113*, 5110-5148; (d) Kiefl, E.; Mannini, M.; Bernot, K.; Yi, X.; Amato, A.; Leviant, T.; Magnani, A.; Prokscha, T.; Suter, A.; Sessoli, R.; Salman, Z. Robust Magnetic Properties of a Sublimable Single-Molecule Magnet. *ACS Nano* **2016**, *10*, 5663-5669; (e) Zhu, Z.; Guo, M.; Li, X.-L.; Tang, J. Molecular magnetism of lanthanide: Advances and perspectives. *Coord. Chem. Rev.* **2019**, *378*, 350-364.

4. (a) Coutinho, J. T.; Monteiro, B.; Pereira, L. C. J. In *Lanthanide-Based Multifunctional Materials*; Martín-Ramos, P., Ramos Silva, M., Ed.; Elsevier: 2018; pp 195-231; (b) Dey, A.; Kalita, P.; Chandrasekhar, V. Lanthanide(III)-Based Single-Ion Magnets.

ACS Omega **2018**, *3*, 9462-9475; (c) Lu, J.; Guo, M.; Tang, J. Recent Developments in Lanthanide Single-Molecule Magnets. *Chem. Asian J.* **2017**, *12*, 2772-2779; (d) Kahn, O. *Molecular Magnetism*. Wiley VCH: 1993.

5. (a) Meihaus, K. R.; Long, J. R. Actinide-based single-molecule magnets. *Dalton Trans.* **2015**, *44*, 2517-2528; (b) Future Directions for Transuranic Single Molecule Magnets. *Inorganics* **2018**, *6*, 26; (c) Coutinho, J. T.; Perfetti, M.; Baldovi, J. J.; Antunes, M. A.; Hallmen, P. P.; Bamberger, H.; Crassee, I.; Orlita, M.; Almeida, M.; van Slageren, J.; Pereira, L. C. J. Spectroscopic Determination of the Electronic Structure of a Uranium Single-Ion Magnet. *Chem. Eur. J.* **2019**, *25*, 1758-1766; (d) King, D. M.; Cleaves, P. A.; Wooles, A. J.; Gardner, B. M.; Chilton, N. F.; Tuna, F.; Lewis, W.; McInnes, E. J. L.; Liddle, S. T. Molecular and electronic structure of terminal and alkali metal-capped uranium(V) nitride complexes. *Nat. Commun.* **2016**, *7*, 13773; (e) Chatelain, L.; Tuna, F.; Pécaut, J.; Mazzanti, M. A zig-zag uranyl(v)–Mn(ii) single chain magnet with a high relaxation barrier. *Chem. Commun.* **2015**, *51*, 11309-11312.

6. (a) Layfield, R. A.; Murugesu, M. *Lanthanides and Actinides in Molecular Magnetism*. Wiley-VCH Verlag GmbH & Co. KGaA 2015; (b) Gao, S. E. *Molecular Nanomagnets and Related Phenomena*. Springer-Verlag Berlin Heidelberg: 2015; (c) Gatteschi, D.; Sessoli, R.; Villain, J. *Molecular Nanomagnets*. 2006.

7. Benelli, C.; Gatteschi, D. *Introduction to Molecular Magnetism: From Transition Metals to Lanthanides*. Wiley-VCH.

8. Bartolomé, E.; Arauzo, A.; Luzón, J.; Bartolomé, J.; Bartolomé, F. In *Handbook of Magnetic Materials*; Brück, E., Ed.; Elsevier: 2017; Vol. 26, pp 1-289.

9. Ishikawa, N.; Sugita, M.; Ishikawa, T.; Koshihara, S.-y.; Kaizu, Y. Lanthanide Double-Decker Complexes Functioning as Magnets at the Single-Molecular Level. *J. Am. Chem. Soc.* **2003**, *125*, 8694-8695.
10. Cotton, S. A. *Lanthanides and Actinides*. Macmillan, London: 1991.
11. (a) Liddle, S. T.; van Slageren, J. Improving f-element single molecule magnets. *Chem. Soc. Rev.* **2015**, *44*, 6655-6669; (b) Chilton, N. F. Design Criteria for High-Temperature Single-Molecule Magnets. *Inorg. Chem.* **2015**, *54*, 2097-2099; (c) Ungur, L.; Chibotaru, L. F. Strategies toward High-Temperature Lanthanide-Based Single-Molecule Magnets. *Inorg. Chem.* **2016**, *55*, 10043-10056; (d) Liu, J.-L.; Chen, Y.-C.; Tong, M.-L. Symmetry strategies for high performance lanthanide-based single-molecule magnets. *Chem. Soc. Rev.* **2018**, *47*, 2431-2453.
12. (a) Day, B. M.; Guo, F.-S.; Layfield, R. A. Cyclopentadienyl Ligands in Lanthanide Single-Molecule Magnets: One Ring To Rule Them All? *Acc. Chem. Res.* **2018**, *51*, 1880-1889; (b) Harriman, K. L. M.; Murugesu, M. An Organolanthanide Building Block Approach to Single-Molecule Magnets. *Acc. Chem. Res.* **2016**, *49*, 1158-1167; (c) Bar, A. K.; Kalita, P.; Singh, M. K.; Rajaraman, G.; Chandrasekhar, V. Low-coordinate mononuclear lanthanide complexes as molecular nanomagnets. *Coord. Chem. Rev.* **2018**, *367*, 163-216.
13. (a) Guo, F.-S.; Day, B. M.; Chen, Y.-C.; Tong, M.-L.; Mansikkamäki, A.; Layfield, R. A. Magnetic hysteresis up to 80 kelvin in a dysprosium metallocene single-molecule magnet. *Science* **2018**, *362*, 1400-1403; (b) Goodwin, C. A. P.; Ortu, F.; Reta, D.; Chilton, N. F.; Mills, D. P. Molecular magnetic hysteresis at 60 kelvin in dysprosocenium. *Nature* **2017**, *548*, 439-442; (c) Guo, F.-S.; Day, B. M.; Chen, Y.-C.; Tong, M.-L.; Mansikkamäki, A.;

Layfield, R. A. A Dysprosium Metallocene Single-Molecule Magnet Functioning at the Axial Limit. *Angew. Chem. Int. Ed.* **2017**, *56*, 11445-11449.

14. Rinehart, J. D.; Long, J. R. Exploiting Single-Ion Anisotropy in the Design of f-Element Single-Molecule Magnets. *Chem. Sci.* **2011**, *2*, 2078-2085.

15. (a) Zhang, P.; Zhang, L.; Wang, C.; Xue, S.; Lin, S.-Y.; Tang, J. Equatorially Coordinated Lanthanide Single Ion Magnets. *J. Am. Chem. Soc.* **2014**, *136*, 4484-4487; (b) Sun, W.-B.; Yan, P.-F.; Jiang, S.-D.; Wang, B.-W.; Zhang, Y.-Q.; Li, H.-F.; Chen, P.; Wang, Z.-M.; Gao, S. High symmetry or low symmetry, that is the question – high performance Dy(III) single-ion magnets by electrostatic potential design. *Chem. Sci.* **2016**, *7*, 684-691; (c) Chen, Y.-C.; Liu, J.-L.; Wernsdorfer, W.; Liu, D.; Chibotaru, L. F.; Chen, X.-M.; Tong, M.-L. Hyperfine-Interaction-Driven Suppression of Quantum Tunneling at Zero Field in a Holmium(III) Single-Ion Magnet. *Angew. Chem. Int. Ed.* **2017**, *56*, 4996-5000; (d) Gupta, S. K.; Murugavel, R. Enriching lanthanide single-ion magnetism through symmetry and axiality. *Chem. Commun.* **2018**, *54*, 3685-3696.

16. (a) Kalita, P.; Acharya, J.; Chandrasekhar, V. Mononuclear pentagonal bipyramidal Ln(III) complexes: Syntheses and magnetic properties. *J. Magn. Magn. Mater.* **2020**, *498*, 166098; (b) Gupta, S. K.; Rajeshkumar, T.; Rajaraman, G.; Murugavel, R. An air-stable Dy(III) single-ion magnet with high anisotropy barrier and blocking temperature. *Chem. Sci.* **2016**, *7*, 5181-5191; (c) Liu, J.; Chen, Y.-C.; Liu, J.-L.; Vieru, V.; Ungur, L.; Jia, J.-H.; Chibotaru, L. F.; Lan, Y.; Wernsdorfer, W.; Gao, S.; Chen, X.-M.; Tong, M.-L. A Stable Pentagonal Bipyramidal Dy(III) Single-Ion Magnet with a Record Magnetization Reversal Barrier over 1000 K. *J. Am. Chem. Soc.* **2016**, *138*, 5441-5450; (d) Jiang, Z.; Sun, L.; Yang, Q.; Yin, B.; Ke, H.; Han, J.; Wei, Q.; Xie, G.; Chen, S. Excess axial electrostatic repulsion as

a criterion for pentagonal bipyramidal DyIII single-ion magnets with high Ueff and TB. *J. Mater. Chem. C* **2018**, *6*, 4273-4280; (e) Ding, Y.-S.; Chilton, N. F.; Winpenny, R. E. P.; Zheng, Y.-Z. On Approaching the Limit of Molecular Magnetic Anisotropy: A Near-Perfect Pentagonal Bipyramidal Dysprosium(III) Single-Molecule Magnet. *Angew. Chem. Int. Ed.* **2016**, *55*, 16071-16074.

17. Bar, A. K.; Kalita, P.; Sutter, J.-P.; Chandrasekhar, V. Pentagonal-Bipyramid Ln(III) Complexes Exhibiting Single-Ion-Magnet Behavior: A Rational Synthetic Approach for a Rigid Equatorial Plane. *Inorg. Chem.* **2018**, *57*, 2398-2401.

18. Pelizzi, C.; Pelizzi, G. Investigation into aroylhydrazones as chelating agents. Synthesis and structural characterization of a tin(IV) complex with 2,6-diacetylpyridine bis(salicyloylhydrazone). *J. Chem. Soc., Dalton Trans.* **1980**, 1970-1973.

19. Sheldrick, G. M. SHELXT-Integrated Space-Group and Crystal-Structure Determination. *Acta Crystallogr., Sect. A: Found. Adv.* **2015**, *71*, 3-8.

20. Sheldrick, G. M. Crystal Structure Refinement with SHELXL. *Acta Crystallogr., Sec. C: Struct. Chem.* **2015**, *71*, 3-8.

21. Dolomanov, O. V.; Bourhis, L. J.; Gildea, R. J.; Howard, J. A. K.; Puschmann, H. OLEX2: a complete structure solution, refinement and analysis program. *J. Appl. Crystallogr.* **2009**, *42*, 339-341.

22. Brandenburg, K.; Putz, H. *DIAMOND*, version 3.2; Crystal Impact GbR: Bonn, Germany, 1997–2014.

23. Aquilante, F.; Autschbach, J.; Carlson, R. K.; Chibotaru, L. F.; Delcey, M. G.; De Vico, L.; Fdez. Galván, I.; Ferré, N.; Frutos, L. M.; Gagliardi, L.; Garavelli, M.; Giussani, A.; Hoyer, C. E.; Li Manni, G.; Lischka, H.; Ma, D.; Malmqvist, P. Å.; Müller, T.; Nenov, A.; Olivucci, M.; Pedersen, T. B.; Peng, D.; Plasser, F.; Pritchard, B.; Reiher, M.; Rivalta, I.; Schapiro, I.; Segarra-Martí, J.; Stenrup, M.; Truhlar, D. G.; Ungur, L.; Valentini, A.; Vancoillie, S.; Veryazov, V.; Vysotskiy, V. P.; Weingart, O.; Zapata, F.; Lindh, R. Molcas 8: New capabilities for multiconfigurational quantum chemical calculations across the periodic table. *J. Comput. Chem.* **2016**, *37*, 506-541.
24. Reiher, M. Relativistic Douglas–Kroll–Hess theory. *Wiley Interdiscip. Rev. Comput. Mol. Sci.* **2012**, *2*, 139-149.
25. (a) *SHAPE: Continuous Shape Measures calculation*, 2.1; Electronic Structure Group, Universitat de Barcelona, Spain, 2013; (b) Cirera, J.; Ruiz, E.; Alvarez, S. Continuous Shape Measures as a Stereochemical Tool in Organometallic Chemistry. *Organometallics* **2005**, *24*, 1556-1562.
26. Ding, Y.-S.; Yu, K.-X.; Reta, D.; Ortu, F.; Winpenny, R. E. P.; Zheng, Y.-Z.; Chilton, N. F. Field- and temperature-dependent quantum tunnelling of the magnetisation in a large barrier single-molecule magnet. *Nat. Commun.* **2018**, *9*, 3134.
27. Li, L.-L.; Su, H.-D.; Liu, S.; Xu, Y.-C.; Wang, W.-Z. A new air- and moisture-stable pentagonal-bipyramidal DyIII single-ion magnet based on the HMPA ligand. *Dalton Trans.* **2019**, *48*, 2213-2219.

28. Chen, Y.-C.; Liu, J.-L.; Ungur, L.; Liu, J.; Li, Q.-W.; Wang, L.-F.; Ni, Z.-P.; Chibotaru, L. F.; Chen, X.-M.; Tong, M.-L. Symmetry-Supported Magnetic Blocking at 20 K in Pentagonal Bipyramidal Dy(III) Single-Ion Magnets. *J. Am. Chem. Soc.* **2016**, *138*, 2829-2837.
29. Chen, Y.-C.; Liu, J.-L.; Lan, Y.; Zhong, Z.-Q.; Mansikkamäki, A.; Ungur, L.; Li, Q.-W.; Jia, J.-H.; Chibotaru, L. F.; Han, J.-B.; Wernsdorfer, W.; Chen, X.-M.; Tong, M.-L. Dynamic Magnetic and Optical Insight into a High Performance Pentagonal Bipyramidal DyIII Single-Ion Magnet. *Chem. Eur. J.* **2017**, *23*, 5708-5715.
30. Guo, Y.-N.; Ungur, L.; Granroth, G. E.; Powell, A. K.; Wu, C.; Nagler, S. E.; Tang, J.; Chibotaru, L. F.; Cui, D. An NCN-pincer ligand dysprosium single-ion magnet showing magnetic relaxation via the second excited state. *Sci. Rep.* **2014**, *4*, 5471.
31. Long, J.; Selikhov, A. N.; Mamontova, E.; Lyssenko, K. A.; Guari, Y.; Larionova, J.; Trifonov, A. A. Single-molecule magnet behaviour in a Dy(iii) pentagonal bipyramidal complex with a quasi-linear Cl–Dy–Cl sequence. *Dalton Trans.* **2019**, *48*, 35-39.
32. Li, M.; Wu, H.; Yang, Q.; Ke, H.; Yin, B.; Shi, Q.; Wang, W.; Wei, Q.; Xie, G.; Chen, S. Experimental and Theoretical Interpretation on the Magnetic Behavior in a Series of Pentagonal-Bipyramidal DyIII Single-Ion Magnets. *Chem. Eur. J.* **2017**, *23*, 17775-17787.
33. (a) Aravena, D.; Ruiz, E. Shedding Light on the Single-Molecule Magnet Behavior of Mononuclear DyIII Complexes. *Inorg. Chem.* **2013**, *52*, 13770-13778; (b) Norre, M. S.; Gao, C.; Dey, S.; Gupta, S. K.; Borah, A.; Murugavel, R.; Rajaraman, G.; Overgaard, J. High-Pressure Crystallographic and Magnetic Studies of Pseudo-D_{5h} Symmetric Dy(III) and

Ho(III) Single-Molecule Magnets. *Inorg. Chem.* **2020**, *59*, 717-729; (c) Dey, S.; Rajaraman, G. In silico design of pseudo D5h actinide based molecular magnets: role of covalency in magnetic anisotropy. *J. Chem. Sci.* **2019**, *131*, 124.

Supporting Information

Table S1. Crystallographic data and refinement parameters of **1–5**.

	1	2	3	4	5
Empirical formula	C ₄₁ H ₅₂ Cl ₁ Gd ₁ N ₅ O ₃ P ₁	C ₈₄ H ₁₁₆ Cl ₂ N ₁₂ O ₈ P ₂ Tb ₂	C ₉₀ H ₁₂₄ Cl ₂ Dy ₂ N ₁₀ O ₈ P ₂	C ₄₁ H ₃₄ Cl ₁ Dy ₁ N ₅ O ₃ P ₁	C ₈₆ H ₁₁₆ Cl ₂ Er ₂ N ₁₀ O ₈ P ₂
Formula weight (g mol ⁻¹)	886.54	1872.56	1931.82	873.65	1885.24
Temperature (K)	120.00(10)	120.00(10)	120(2)K	120(2)	120.00(10)
Crystal system	Monoclinic	Triclinic	Monoclinic	Triclinic	Monoclinic
Space group	P21/n	P-1	P21/c	P-1	P21/n
Unit cell lengths (Å)	a = 20.1164(5) b = 9.6283(2) c = 22.3601(6)	a = 10.0872(3) b = 18.3148(5) c = 23.4884(6)	a = 18.6952(5) b = 9.9898(3) c = 24.5545(7)	a = 8.8046(2) b = 11.5978(2) c = 18.9669(3)	a = 23.5494(8) b = 10.0618(3) c = 36.0847(11)
Unit cell angles (°)	β = 113.594(3)	α = 84.704(2) β = 89.758(2) γ = 83.504(2)	β = 91.430(2)	α = 93.4930(10) β = 101.8670(10) γ = 103.418(2)	β = 94.409(3)
Volume (Å ³)	3968.81(19)	4293.0(2)	4584.4(2)	1831.60(6)	8524.9(5)
Z	4	2	2	2	8
Density (calculated)	1.484	1.449	1.399 mg/m ³	1.584	1.469
Absorption coefficient	1.823	1.794	1.769 mm ⁻¹	2.203	2.116
F(000)	1812.0	1924.0	1988.0	874.0	3864.0
Crystal size (mm)	0.17 × 0.14 × 0.1	0.18 × 0.14 × 0.07	0.3 × 0.08 × 0.01 mm ³	0.34 × 0.11 × 0.09	0.21 × 0.12 × 0.09
2θ range for data collection (°)	5.5 to 58.818	5.244 to 49.998	5.412 to 57.664°	4.884 to 58.042	4.892 to 58.068
Reflections collected	62624	91078	53867	27626	96210
Index ranges	-27 ≤ h ≤ 24, -11 ≤ k ≤ 12, -30 ≤ l ≤ 27	-11 ≤ h ≤ 11, -21 ≤ k ≤ 21, -27 ≤ l ≤ 27	-24 ≤ h ≤ 23, -13 ≤ k ≤ 8, -33 ≤ l ≤ 30	-11 ≤ h ≤ 9, -15 ≤ k ≤ 15, -24 ≤ l ≤ 24	-30 ≤ h ≤ 32, -13 ≤ k ≤ 13, -45 ≤ l ≤ 44
Independent reflections	9730 [R _{int} = 0.0382]	15077 [R _{int} = 0.0576]	10841 [R _{int} = 0.0587]	8459 [R _{int} = 0.0448]	19876 [R _{int} = 0.0840]
Data/Restrain/Parameter	9730/0/471	15077/0/999	10841/0/518	8459/0/471	19876/0/999
Goodness-of-fit on F ²	1.031	1.159	1.040	1.055	1.026
Final R indices [I > 2σ(I)]	R ₁ = 0.0228, wR ₂ = 0.0448	R ₁ = 0.0492, wR ₂ = 0.1197	R ₁ = 0.0346, wR ₂ = 0.0644	R ₁ = 0.0293, wR ₂ = 0.0648	R ₁ = 0.0470, wR ₂ = 0.0936
R indices (all data)	R ₁ = 0.0289, wR ₂ = 0.0465	R ₁ = 0.0549, wR ₂ = 0.1223	R ₁ = 0.0571, wR ₂ = 0.0704	R ₁ = 0.0348, wR ₂ = 0.0668	R ₁ = 0.0898, wR ₂ = 0.1079
$R_1 = \sum F_o - F_c / \sum F_o; wR_2 = \sum [w(F_o^2 - F_c^2)]^2 / [w(F_o^2)]^{\frac{1}{2}}$					

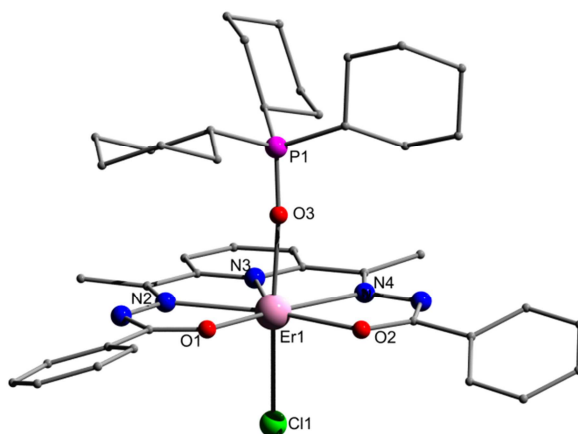


Figure S4. Molecular structure of complex **5**. (H-atoms are omitted for clarity)

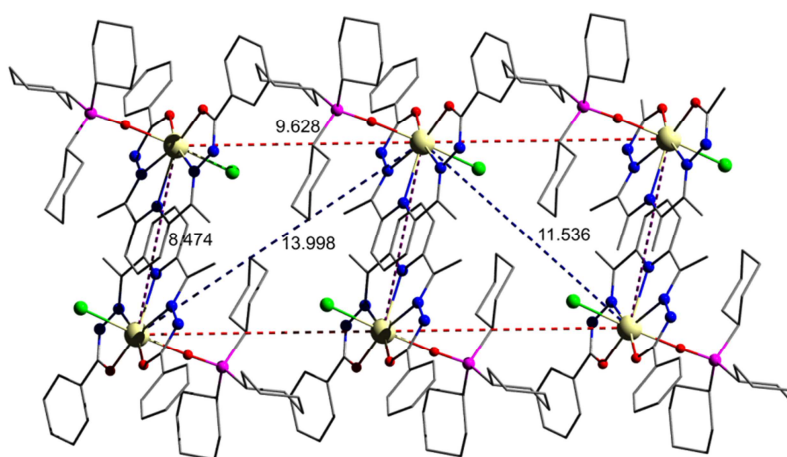


Figure S5. Solid-state packing diagram of complex **1** viewed along the crystallographic *c* axis. (H-atoms are omitted for clarity)

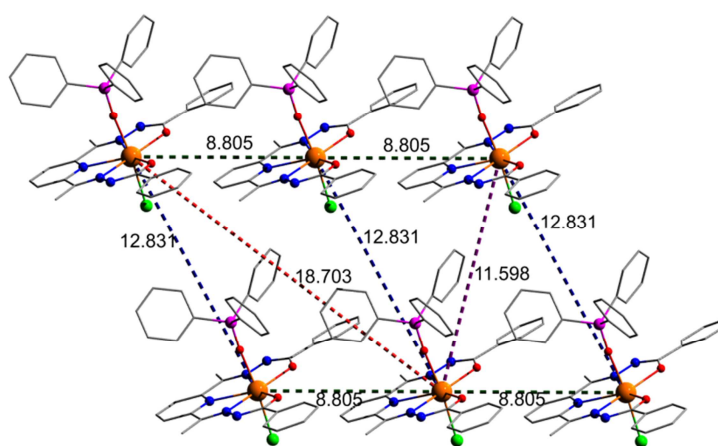


Figure S6. Solid-state packing diagram of complex **4** viewed along the crystallographic *c* axis (H-atoms are omitted for clarity).

Table 2. Bond distance and bond angle parameters of complex **3**.

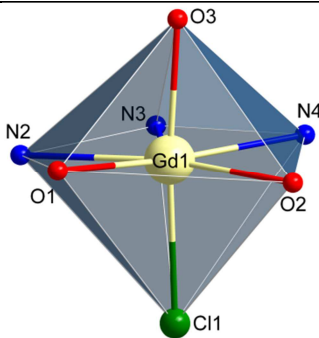
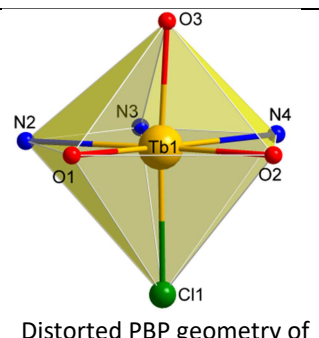
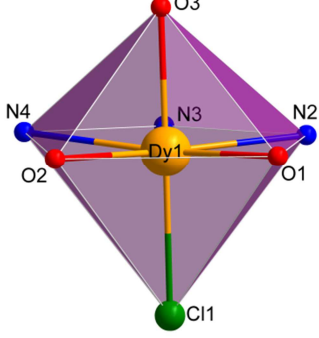
Bond distances (Å)		Bond angles (°)			
Dy1-Cl1	2.625(8)	O2-Dy1-Cl1	93.19(5)	O2-Dy1-O1	100.23(7)
Dy1-O1	2.272(2)	O2-Dy1-N3	130.25(7)	O2-Dy1-N2	165.17(7)
Dy1-O2	2.259(2)	O2-Dy1-N4	65.59(7)	O3-Dy1-Cl1	169.62(5)
Dy1-O3	2.237(2)	O3-Dy1-O1	92.19(7)	O3-Dy1-O2	90.35(7)
Dy1-N3	2.462(2)	O3-Dy1-N3	84.83(7)	O3-Dy1-N2	91.41(7)
Dy1-N2	2.464(2)	O3-Dy1-N4	81.19(7)	N3-Dy1-Cl1	85.44(6)
Dy1-N4	2.448(2)	N3-Dy1-N2	64.57(7)	N2-Dy1-Cl1	87.67(6)
		O1-Dy1-Cl1	96.78(6)	O1-Dy1-N3	129.37(7)
		O1-Dy1-N2	65.00(7)	O1-Dy1-N4	164.10(7)
		N4-Dy1-Cl1	91.39(6)	N4-Dy1-N3	64.74(7)

Table S3. Continuous shape analysis

Complex	Structure ¹						
	HP-7	HPY-7	PBPY-7	COC-7	CTPR-7	JPBPY-7	JETPY-7
1	31.572	19.350	2.233	7.665	6.207	6.298	18.718
2	32.740	20.143	1.732	7.872	6.409	5.652	20.810
3	32.944	22.380	1.446	8.229	6.678	5.549	21.175
4	32.742	21.540	1.505	7.661	6.338	5.725	21.267
5	32.781	20.809	1.353	7.774	6.403	5.232	21.450

¹HP-7: Heptagon (D_{7h}); HPY-7: Hexagonal pyramid (C_{6v}); PBPY-7: Pentagonal bipyramid (D_{5h}); COC-7: Capped octahedron (C_{3v}); CTPR-7: Capped trigonal prism (C_{2v}); JPBPY-7: Johnson pentagonal bipyramid J13 (D_{5h}); JETPY-7: Johnson elongated triangular pyramid J7 (C_{3v})

Table S4. Crystallographic details of **1**, **2**, **4** and **5**.

Coordination geometry	Bond lengths (Å)	Bond angles (°)
 <p>Distorted PBP geometry of Gd^{III} center in 1</p>	Gd1–Cl1 2.645(5) Gd1–O1 2.330(12) Gd1–O2 2.313(12) Gd1–O3 2.271(13) Gd1–N3 2.510(15) Gd1–N2 2.522(15) Gd1–N4 2.480(15)	O1–Gd1–Cl1 97.10(3) O1–Gd1–N3 126.15(4) O1–Gd1–N2 63.55(5) O1–Gd1–N4 167.95(5) O2–Gd1–Cl1 87.60(3) O2–Gd1–O1 105.63(4) O2–Gd1–N3 128.20(5) O2–Gd1–N2 167.59(5) O2–Gd1–N4 64.78(5) O3–Gd1–Cl1 174.67(3) O3–Gd1–O1 87.87(5) O3–Gd1–O2 89.22(5) O3–Gd1–N3 91.00(5) O3–Gd1–N2 96.12(5) O3–Gd1–N4 84.82(5) N3–Gd1–Cl1 87.61(3) N3–Gd1–N2 63.08(5) N2–Gd1–Cl1 87.84(4) N4–Gd1–Cl1 89.96(4) N4–Gd1–N3 63.68(5)
 <p>Distorted PBP geometry of Tb^{III} center in 2</p>	Tb1–Cl1 2.622(12) Tb1–O1 2.291(3) Tb1–O2 2.306(3) Tb1–O3 2.228(4) Tb1–N4 2.472(4) Tb1–N3 2.500(4) Tb1–N2 2.495(4)	O1–Tb1–Cl1 93.57(10) O1–Tb1–O2 102.50(13) O1–Tb1–N4 167.36(13) O1–Tb1–N3 128.57(13) O1–Tb1–N2 64.66(14) O2–Tb1–Cl1 90.53(10) O2–Tb1–N4 65.20(13) O2–Tb1–N3 128.85(13) O2–Tb1–N2 167.16(14) O3–Tb1–Cl1 175.22(9) O3–Tb1–O1 91.19(13) O3–Tb1–O2 87.95(13) O3–Tb1–N4 85.66(13) O3–Tb1–N3 88.25(13) O3–Tb1–N2 92.04(13) N4–Tb1–Cl1 89.59(10) N4–Tb1–N3 63.65(13) N4–Tb1–N2 127.62(14) N3–Tb1–Cl1 89.18(10) N2–Tb1–Cl1 90.44(10)
 <p>Distorted PBP geometry of Dy^{III} center in 4</p>	Dy1–Cl1 2.622(7) Dy1–O2 2.282(2) Dy1–O3 2.276(2) Dy1–O1 2.285(2) Dy1–N4 2.456(2) Dy1–N2 2.457(2) Dy1–N3 2.467(2)	O2–Dy1–Cl1 94.12(5) O2–Dy1–O1 100.00(6) O2–Dy1–N4 65.20(7) O2–Dy1–N2 164.01(7) O2–Dy1–N3 129.84(7) O3–Dy1–Cl1 174.07(5) O3–Dy1–O2 89.99(7) O3–Dy1–O1 88.02(6) O3–Dy1–N4 88.02(7) O3–Dy1–N2 83.31(7) O3–Dy1–N3 85.96(7) O1–Dy1–Cl1 95.46(5) O1–Dy1–N4 164.67(7) O1–Dy1–N2 65.38(7) O1–Dy1–N3 129.71(7) N4–Dy1–Cl1 89.83(5) N4–Dy1–N2 128.73(8) N4–Dy1–N3 64.71(8) N2–Dy1–Cl1 93.75(5) N2–Dy1–N3 64.32(7)

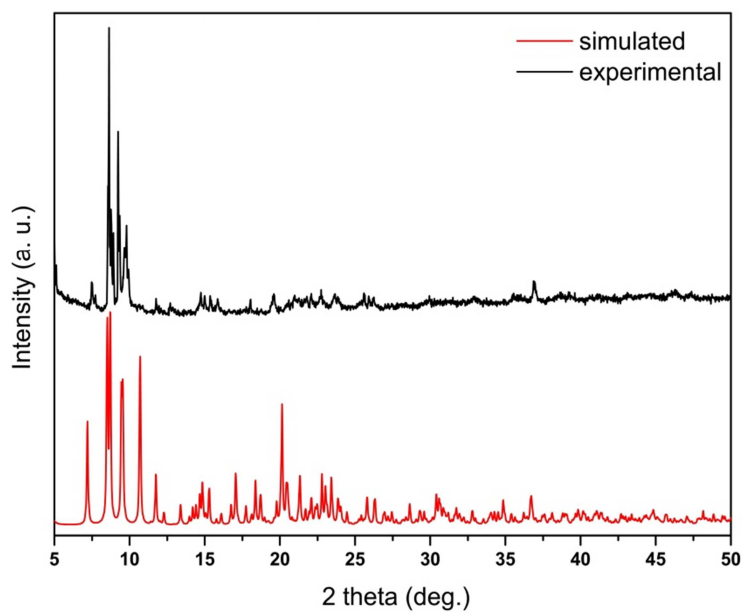
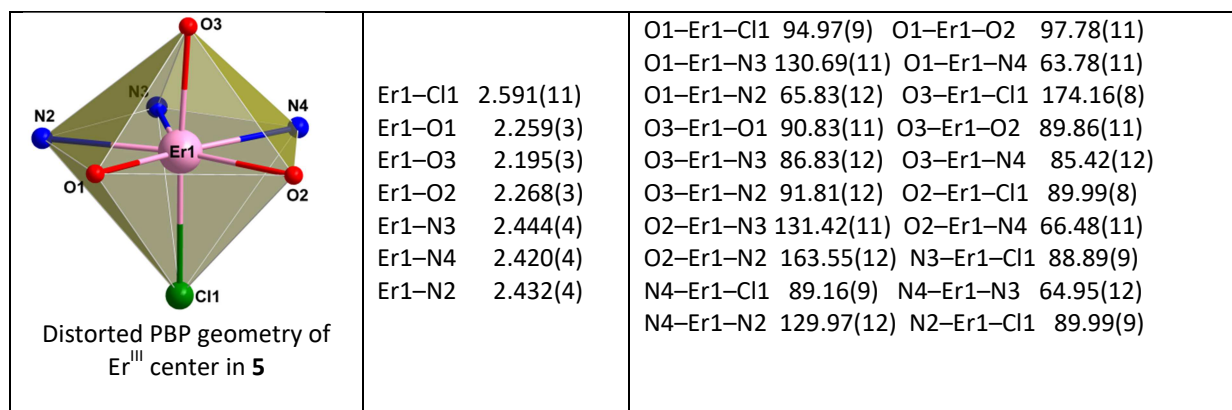


Figure S7. The experimental and simulated powder XRD pattern of complex **3'**.

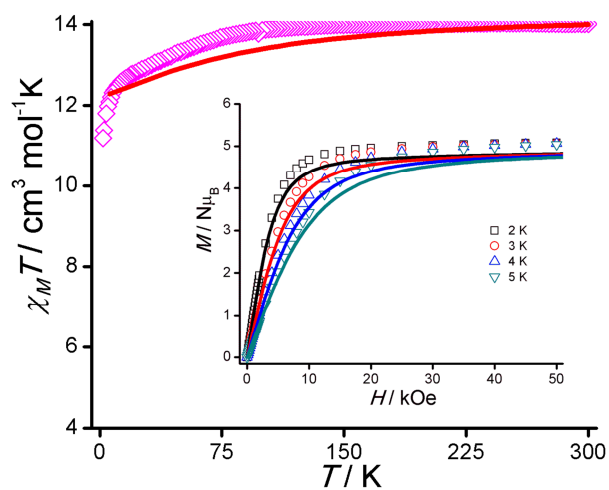


Figure S8. Magnetic behavior for **4**. (a) Temperature dependence of $\chi_M T$ and (b) field dependence of the magnetization (inset), solid lines represent the *ab initio* computed data using MOLCAS 8.2 program.

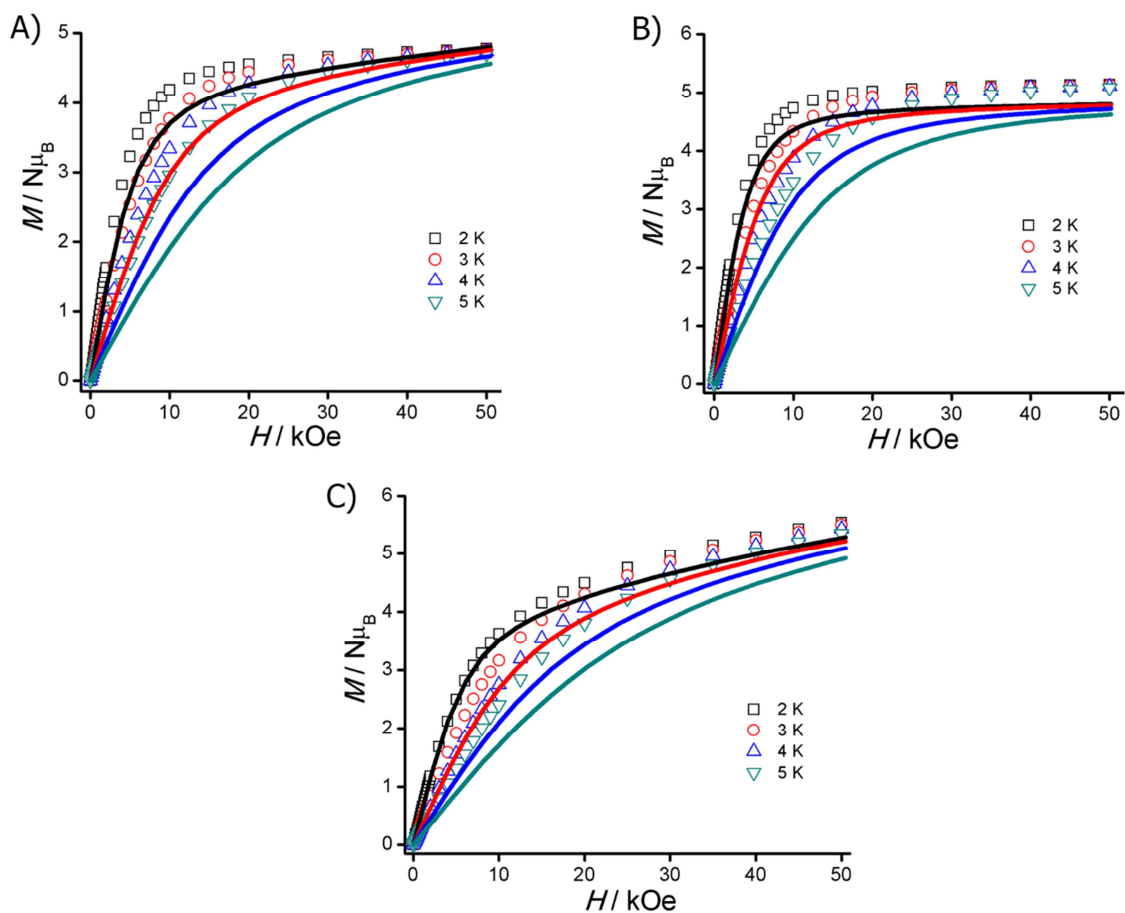
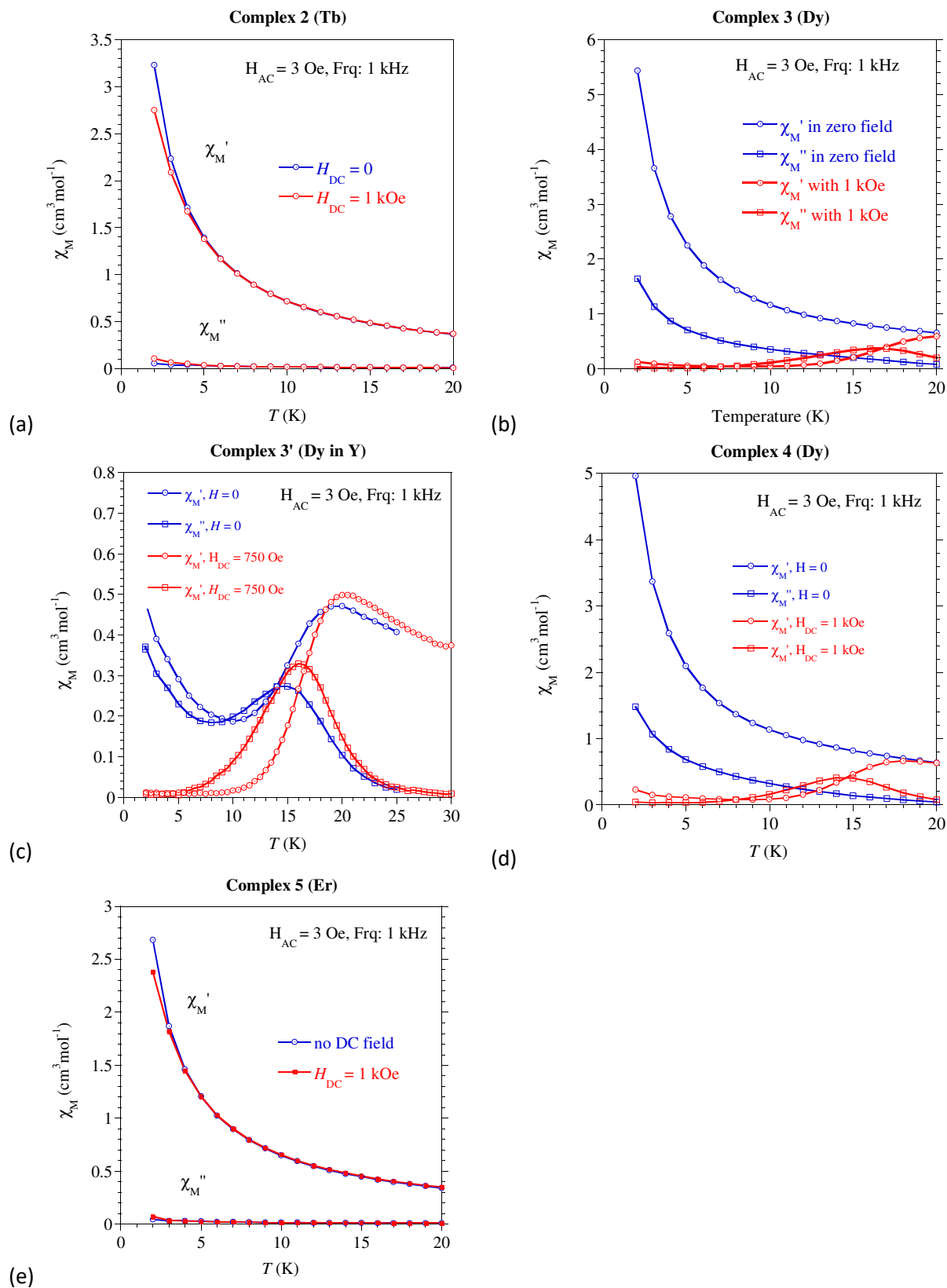


Figure S9. Field dependence of the magnetization (A-C) for complexes **2-3** and **5** respectively, solid lines are the *ab initio* computed data using MOLCAS 8.2 program.

Figure S140. temperature dependence of the AC susceptibility in zero field and in an applied field of 1 kOe or 750 Oe for **2** (a), **3** (b), **3'** (c), **4** (c), and **5** (e).



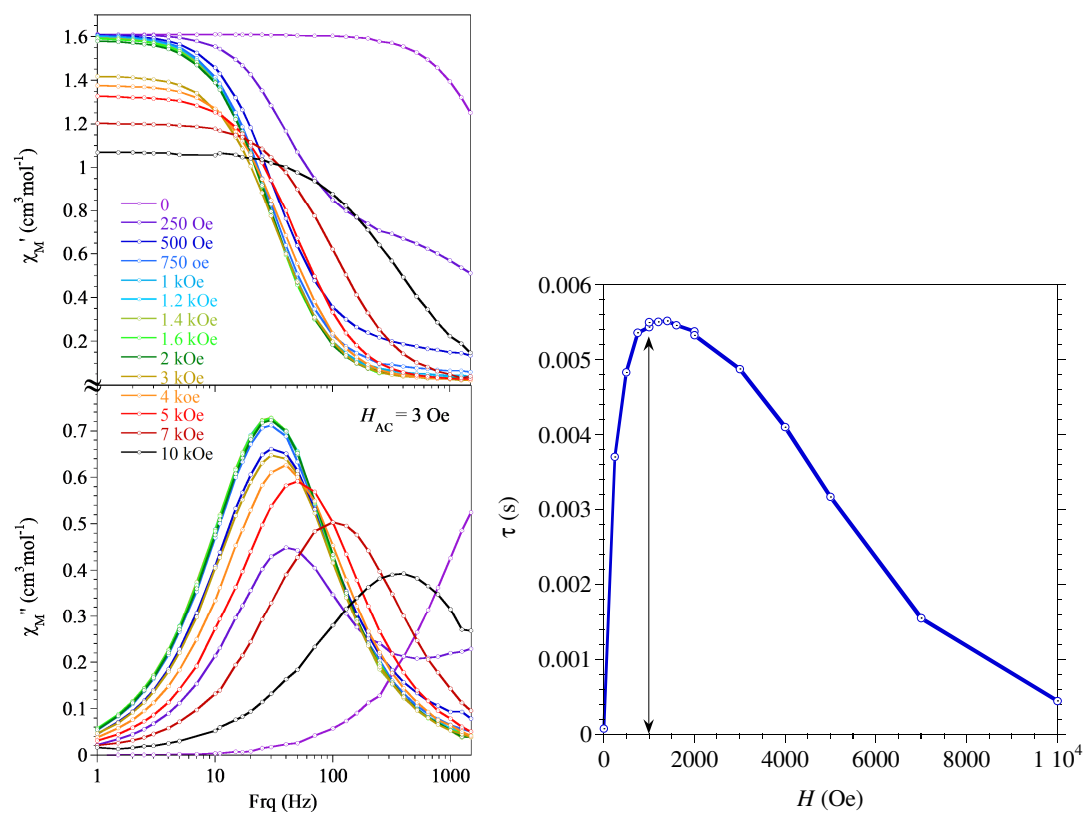


Figure S10. Field dependence of the AC susceptibility (*left*), and of the relaxation time, τ (*right*), for **3** at 8 K. The larger τ is reached for 1 kOe which was used as applied DC field in the AC studies for this complex.

Table S5. Best fit parameters of the Debye model to the $\chi''_{\text{M}} = f(\text{frq})$ behaviors for **3**. χ_{T} stands for the isothermal susceptibility, χ_{s} for the adiabatic susceptibility, τ for the relaxation time, and α accounts for the distribution width of the relaxation time.

T (K)	χ_{T}	χ_{s}	τ (s)	α
4.5	5.71	3.29	0.11675	0.12
5.0	5.61	3.39	0.065181	0.12
5.5	5.52	3.47	0.038369	0.11
6.0	5.45	3.55	0.024021	0.10
6.5	5.38	3.61	0.015912	0.095
7.0	5.33	3.67	0.011003	0.088
7.5	5.28	3.72	0.007867	0.082
8.0	5.24	3.76	0.005804	0.078
8.5	5.20	3.80	0.004379	0.075
9.0	5.16	3.84	0.003369	0.073
9.5	5.13	3.87	0.002638	0.070
10.0	5.10	3.90	0.002096	0.068
10.5	5.07	3.93	0.001685	0.065
11.0	5.05	3.95	0.001365	0.065
11.5	5.02	3.97	0.001128	0.064
12.0	5.00	4.00	0.000905	0.063
12.5	4.98	4.01	0.00075741	0.060
13.0	4.97	4.03	0.0006327	0.059
13.5	4.95	4.05	0.00053185	0.057
14.0	4.94	4.06	0.00044954	0.056
14.5	4.92	4.08	0.00037815	0.056
15.0	4.91	4.09	0.00031952	0.055
15.5	3.90	3.10	0.00027045	0.055
16.0	3.88	3.11	0.00022847	0.052
16.5	3.87	3.13	0.00019351	0.050
17.0	3.86	3.14	0.0001633	0.048
17.5	4.35	3.65	0.00013939	0.042
18.0	3.84	3.16	0.00011626	0.041

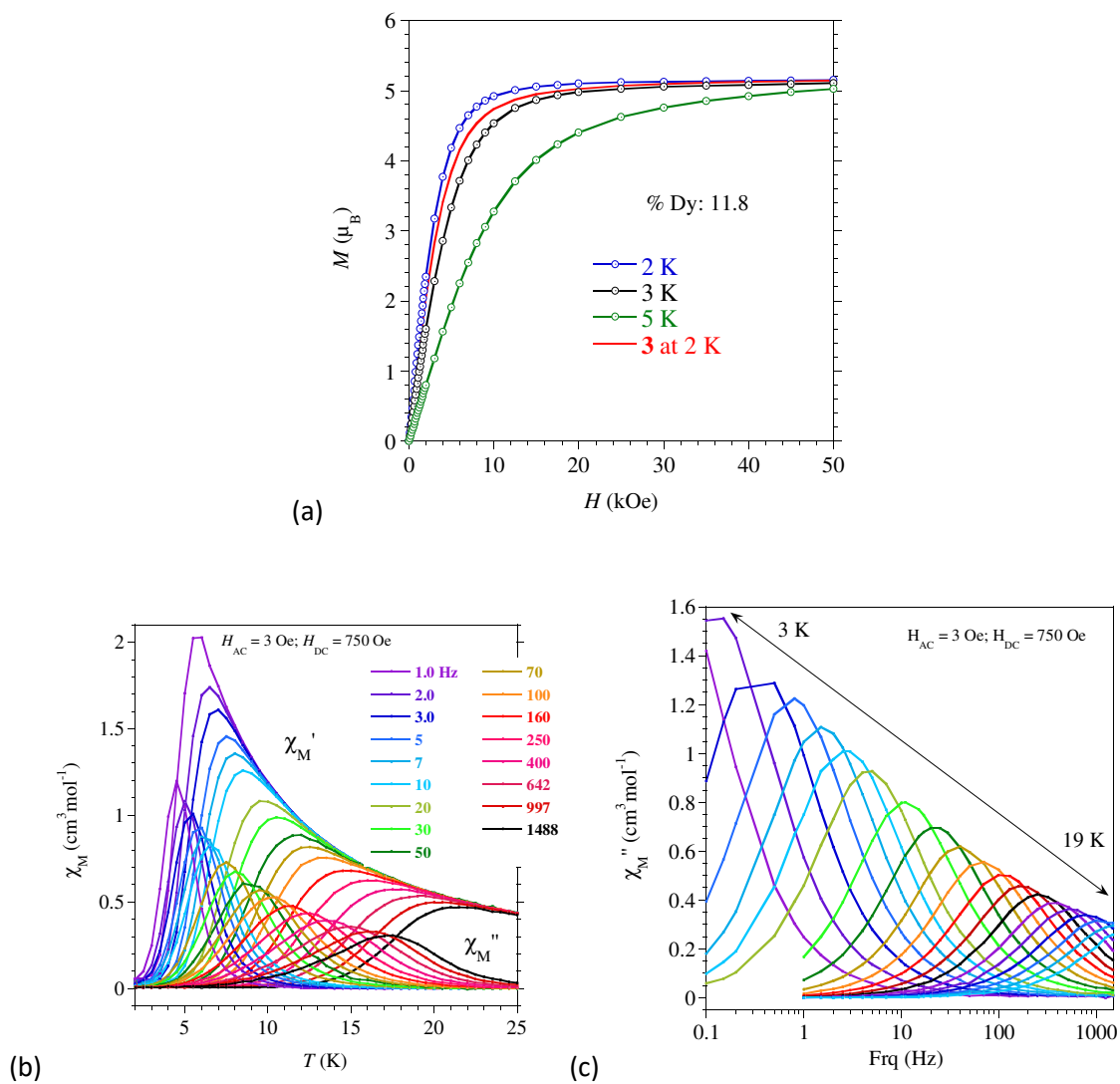


Figure S12. Magnetic behavior for **3'**. The composition in Dy^{III} for the sample was estimated by adjusting the magnetization reached for **3'** under 5 t at 2 K (blue plot in (a)) to that of **3** at same temperature (red plot).

Table S4. Best fit parameters of the Debye model to the $\chi''_{\text{M}} = f(\text{frq})$ behaviors for **3'**. χ_{T} stands for the isothermal susceptibility, χ_{S} for the adiabatic susceptibility, τ for the relaxation time, and α accounts for the distribution width of the relaxation time.

T (K)	χ_{T}	χ_{S}	τ (s)	α
4.0	5.825	3.175	0.166	0.16
4.5	5.6816	3.3184	0.080	0.11
5.0	5.5944	3.4056	0.04511	0.062
5.5	5.5049	3.4951	0.02776	0.064
6.0	5.4324	3.5677	0.0178	0.0558
6.5	5.3645	3.6355	0.01177	0.0573
7.0	5.3137	3.6863	0.00817	0.052
7.5	5.2669	3.7331	0.00577	0.048
8.0	5.2233	3.7767	0.00417	0.044
8.5	5.1878	3.8122	0.00306	0.034
9.0	5.1514	3.8486	0.00230	0.035
9.5	5.119	3.881	0.001747	0.037
10.0	5.0922	3.9078	0.001341	0.027
10.5	5.0658	3.9342	0.001049	0.032
11.0	5.0435	3.9565	0.000825	0.026
11.5	5.0224	3.9776	0.000656	0.023
12.0	5.001	3.999	0.000517	0.018
12.5	4.9822	4.0178	0.000421	0.023
13.0	4.9661	4.0339	0.0003419	0.020
13.5	4.9513	4.0487	0.0002823	0.011
14.0	4.9367	4.0633	0.000233	0.008
14.5	4.9235	4.0765	0.0001895	0.013
15.0	4.9127	4.0873	0.000156	0.01
15.5	4.9004	4.0996	0.000128	6e-5
16.0	4.89	4.11	0.0001045	0.002
16.5	4.8769	4.1231	8.57e-5	0.0005

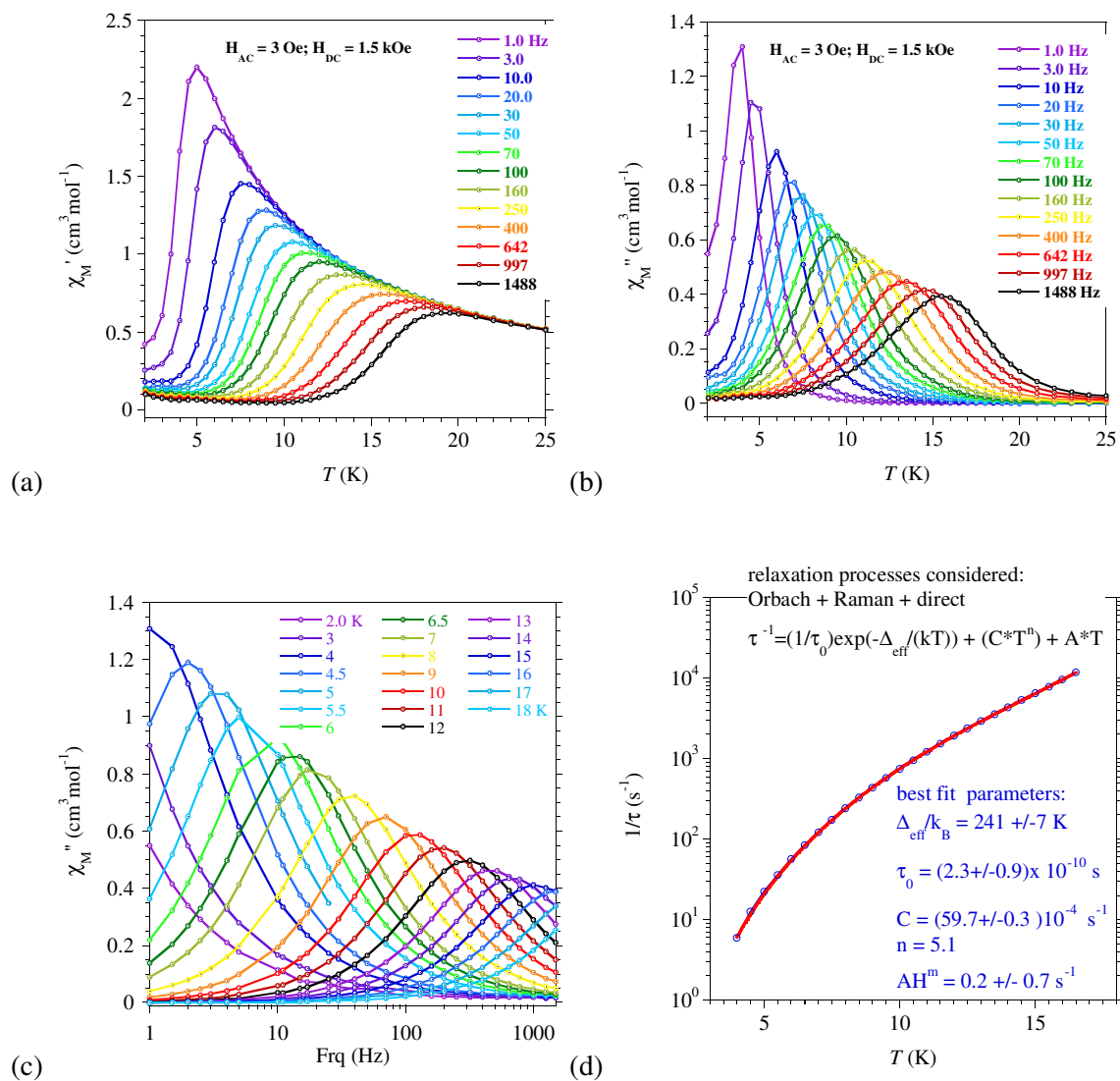


Figure S12. AC susceptibility behavior for 4.

Table S7. Best fit parameters of the Debye model to the $\chi''_M = f(\text{freq})$ behaviors for **4**. χ_T stands for the isothermal susceptibility, χ_s for the adiabatic susceptibility, τ for the relaxation time, and α accounts for the distribution width of the relaxation time.

T (K)	χ_T	χ_s	τ (s)	α
4.0	5.825	3.175	0.166	0.16
4.5	5.6816	3.3184	0.080	0.11
5.0	5.5944	3.4056	0.04511	0.062
5.5	5.5049	3.4951	0.02776	0.064
6.0	5.4324	3.5677	0.0178	0.0558
6.5	5.3645	3.6355	0.01177	0.0573
7.0	5.3137	3.6863	0.00817	0.052
7.5	5.2669	3.7331	0.00577	0.048
8.0	5.2233	3.7767	0.00417	0.044
8.5	5.1878	3.8122	0.00306	0.034
9.0	5.1514	3.8486	0.00230	0.035
9.5	5.119	3.881	0.001747	0.037
10.0	5.0922	3.9078	0.001341	0.027
10.5	5.0658	3.9342	0.001049	0.032
11.0	5.0435	3.9565	0.000825	0.026
11.5	5.0224	3.9776	0.000656	0.023
12.0	5.001	3.999	0.000517	0.018
12.5	4.9822	4.0178	0.000421	0.023
13.0	4.9661	4.0339	0.0003419	0.020
13.5	4.9513	4.0487	0.0002823	0.011
14.0	4.9367	4.0633	0.000233	0.008
14.5	4.9235	4.0765	0.0001895	0.013
15.0	4.9127	4.0873	0.000156	0.01
15.5	4.9004	4.0996	0.000128	6e-5
16.0	4.89	4.11	0.0001045	0.002
16.5	4.8769	4.1231	8.57e-5	0.0005

Table S8. Basis set used for all the elements in our calculation.

Elements	Basis set
H	H.ANO-RCC...2s.
C	C.ANO-RCC...3s2p.
N	N.ANO-RCC...4s3p2d1f.
O	O.ANO-RCC...4s3p2d1f.
P	P.ANO-RCC...4s3p.
Cl	Cl.ANO-RCC...5s4p2d1f.
Tb	Tb.ANO-RCC...8s7p5d3f2g1h.
Dy	Dy.ANO-RCC...7s6p4d2f1g.

Er	Er.ANO-RCC...8s7p5d3f2g1h.
----	----------------------------

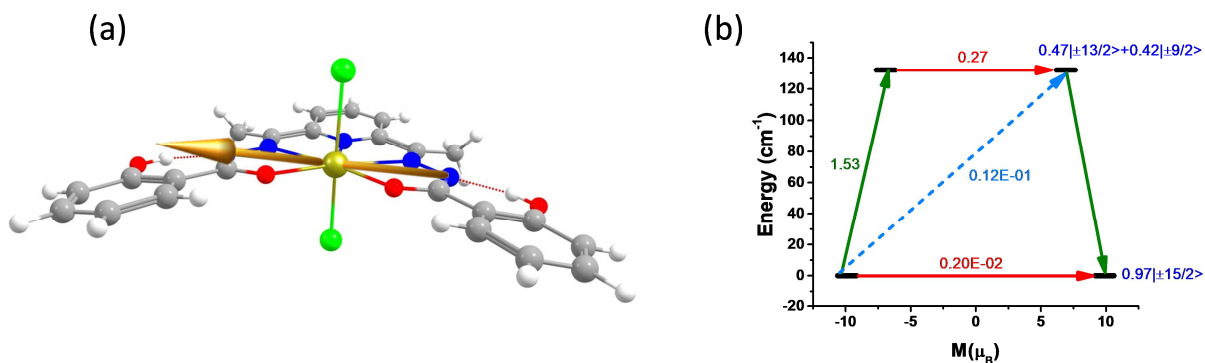


Figure S14. Computed g_{zz} orientation in complex **6** (a) and possible magnetization relaxation pathways (b). The red arrows show the QTM and TA-QTM via ground and higher excited KD respectively. The sky dotted arrows show the Orbach process for the relaxation. The green arrows show the possible mechanism of magnetic relaxation. The blue characters imply the m_j composition of the KDs.

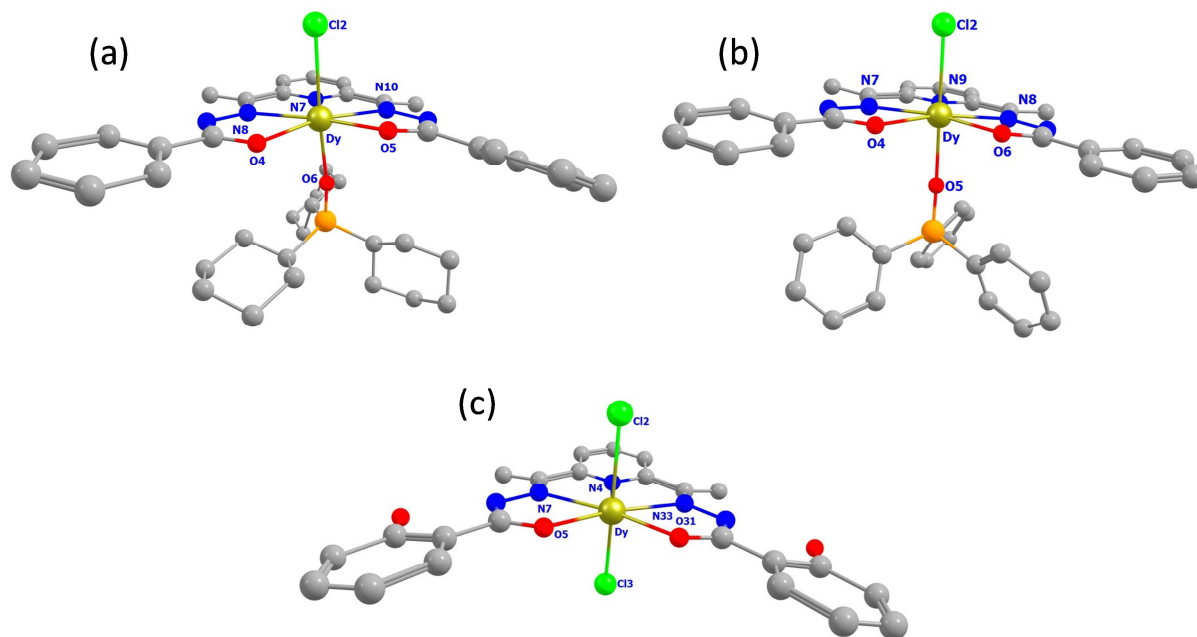


Figure S15. Atom number for Loprop charge of complex (A) **3** (B) **4** (C) **6**. Colour code: Dy-greenish yellow, Cl-green, P-violet, O-red, N-blue, C-grey. Hydrogens are removed for clarity.

Table S9. LoProp charge of the metal center and its coordinated atom of complex **3**, **4** and **6**.

Atom	3	4	6
Dy	2.5006	2.4993	2.4656
O6/O5/Cl1	-1.1346	-1.1107	-0.8799
Cl2	-0.8781	-0.8753	-0.8713
O4/O4/O5	-0.8314	-0.8228	-0.8236
O5/O6/O31	-0.8242	-0.8283	-0.8239
N7/N7/N4	-0.3882	-0.2262	-0.3726
N8/N8/N7	-0.2568	-0.2542	-0.2660
N10/N9/N33	-0.2497	-0.3908	-0.2662
Av. axial/av. Equatorial	1.9730	1.9684	1.7153

Table S10. The *ab initio* computed crystal field parameter of complex **3**, **4** and **6**.

k	Q	B_k^q		
		3	4	6
2	-2	1.20E-01	-1.63E-02	-1.52E-02
	-1	-5.59E-02	-2.09E-02	1.34E-02
	0	-2.18E+00	-2.32E+00	-2.80E+00
	1	-1.13E-01	-7.01E-01	4.89E-03
	2	-2.14E-01	2.34E-01	1.77E+00
4	-4	1.70E-02	-2.97E-03	1.26E-03
	-3	3.73E-04	-5.85E-04	4.58E-04
	-2	-1.22E-02	2.32E-03	-8.19E-05
	-1	-3.69E-04	-1.81E-04	1.91E-04
	0	-1.57E-03	-1.41E-03	-8.93E-04
	1	-7.93E-04	2.33E-03	-2.42E-07
	2	4.28E-02	4.22E-02	4.04E-02
	3	6.25E-03	-2.79E-03	-7.15E-05
4	-3.02E-02	-3.35E-02	-2.75E-02	
6	-6	-4.13E-05	2.50E-05	1.59E-05
	-5	-8.33E-06	1.29E-05	-1.89E-06
	-4	-2.58E-05	2.40E-05	8.27E-06
	-3	4.59E-05	1.16E-05	-4.35E-06
	-2	7.59E-05	2.63E-05	2.53E-05
	-1	3.82E-05	1.42E-05	-7.95E-06
	0	-5.50E-05	-5.30E-05	-4.64E-05
	1	9.50E-06	2.02E-05	-4.09E-07
	2	-4.03E-04	-4.02E-04	-4.20E-04
	3	-7.82E-05	-3.79E-05	3.72E-07
	4	6.56E-06	7.68E-06	5.92E-05
5	3.19E-05	6.33E-05	-3.51E-07	
6	-1.06E-05	3.32E-05	-4.81E-05	

Table S11. The *ab initio* computed energy and the associated g-tensors of the low lying KDs generated from ${}^6\text{H}_{15/2}$ state of complexes **3a**, **4a** and **6a**.

Energy (K)	g_x	g_y	g_z	Angle of g_{zz} between ground and higher excited states (°)
Complex 3a				
0.0	0.000	0.000	20.019	
800.9	0.000	0.000	17.033	0.10
1541.7	0.002	0.002	14.169	0.21
2141.7	0.020	0.022	11.502	0.94
2540.6	0.531	0.554	8.987	3.32
2748.4	0.145	0.914	6.536	10.87
2829.7	7.252	6.383	3.190	6.36
2864.3	0.768	3.319	16.642	89.83
Complex 4a				
0.0	0.000	0.000	20.011	
777.5	0.000	0.000	17.036	0.05
1498.5	0.002	0.002	14.178	0.12
2082.8	0.017	0.020	11.210	0.30
2471.6	0.535	0.555	8.984	0.83
2674.8	0.263	0.810	6.456	2.52
2754.0	7.353	6.364	3.297	1.32
2787.4	0.722	3.008	16.723	89.94
Complex 6a				
0.0	0.000	0.000	20.011	
712.9	0.000	0.000	17.066	0.14
1362.0	0.009	0.010	14.234	0.22
1886.7	0.065	0.083	11.553	0.29
2248.4	1.525	1.581	8.899	0.51
2459.8	0.761	2.190	6.268	1.54
2555.0	7.933	7.690	3.001	0.80
2616.8	0.510	1.867	17.633	90.00

Table S12. LoProp charge of the metal center and its coordinated atom of complex **3a**, **4a** and **6a**.

Atom	3a	4a	6a
Dy	2.6301	2.6357	2.5568
O6/O5/Cl1	-1.2234	-1.2172	-0.7804
Cl2	-0.7576	-0.7519	-0.7764

Table S13. The *ab initio* computed crystal field parameter of complex **3a**, **4a** and **6a**.

k	Q	B_k^q		
		3a	4a	6a
2	-2	9.10E-02	2.95E-02	3.18E-07
	-1	-9.54E-02	6.71E-02	-2.31E-08
	0	-1.21E+01	-1.18E+01	-1.10E+01
	1	5.94E-02	-1.57E-02	9.50E-02
	2	2.24E-01	1.81E-01	-4.22E-01
4	-4	-2.18E-04	-8.87E-06	-3.74E-09
	-3	-1.11E-03	6.57E-04	5.79E-10
	-2	1.22E-04	-1.63E-05	-8.69E-10
	-1	1.82E-03	-5.31E-04	1.48E-10
	0	-6.49E-03	-6.26E-03	-4.60E-03
	1	-3.44E-04	4.15E-05	-4.11E-04
	2	-4.40E-04	-7.07E-04	1.10E-03
	3	1.62E-04	2.90E-04	-5.07E-04
6	4	-1.44E-03	-1.42E-03	2.49E-03
	-6	7.25E-06	4.93E-07	2.17E-10
	-5	-1.04E-05	4.44E-06	-2.51E-10
	-4	-3.17E-06	-1.78E-07	-6.33E-11
	-3	-6.28E-06	4.31E-06	3.35E-11
	-2	-3.51E-06	1.24E-07	3.57E-12
	-1	-1.95E-05	1.86E-06	4.14E-13
	0	4.16E-05	4.05E-05	2.85E-05
	1	-2.99E-06	1.34E-06	-4.29E-06
	2	-1.31E-06	4.71E-06	-5.29E-06
	3	-3.64E-06	-1.01E-06	-3.47E-05
	4	-2.27E-05	-2.39E-05	4.47E-05
	5	1.68E-05	-2.43E-06	1.39E-04
	6	3.38E-05	3.37E-05	-1.02E-04

Table S14. The *ab initio* computed energy with the associated g-tensors and tunneling splitting (Δ_{tun}) of the low lying energy levels of complexes **2**.

Levels	Energy (K)	g_{zz}	Δ_{tun}
1	0	16.69	1.88
2	2.7072		
3	64.8432	13.745	4.82
4	71.784		
5	261.72	10.003	8.98
6	274.6512		
7	550.5984	14.163	13.08
8	569.4336		

Table S15. The *ab initio* computed energy (cm^{-1}) with the associated g-tensors of the eight low lying KDs of complexes **5**.

Complex 5			
Energy (K)	g_x	g_y	g_z
0.0	0.089	1.396	14.176
20.7	1.608	3.471	12.510
50.3	0.220	4.998	11.662
185.5	3.176	4.926	9.333
320.7	0.882	2.076	12.297
403.1	1.227	3.722	14.512
610.4	0.026	0.672	15.353
632.3	0.229	0.671	15.370

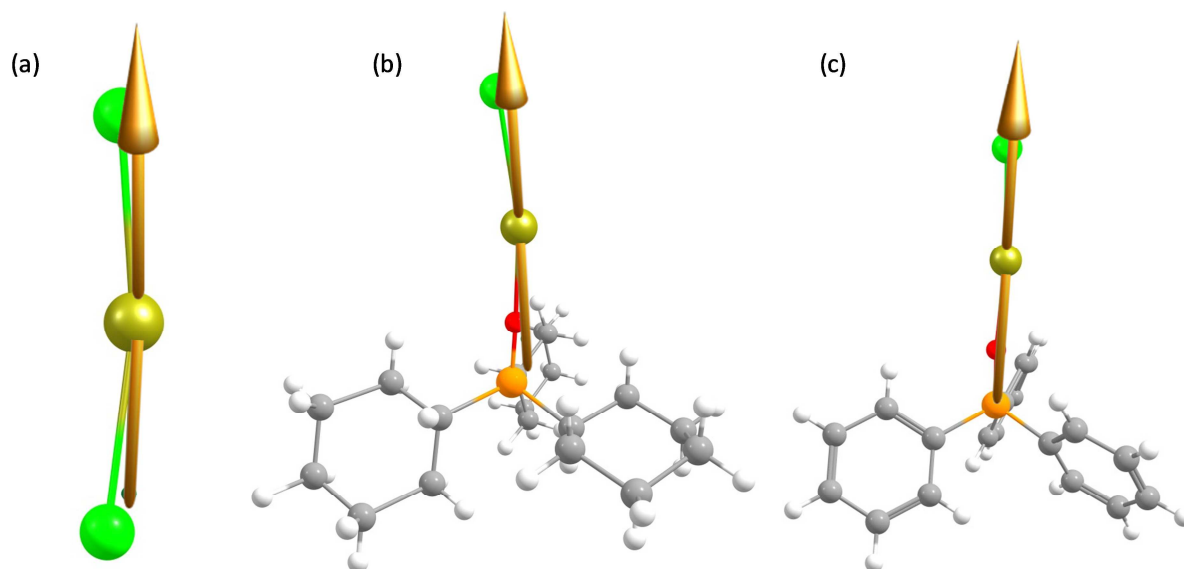


Figure S16. (a) Anisotropy axis of **3a**. (b) Anisotropy axis of **4a**. (c) Anisotropy axis of **6a**. Colour code: Dy-greenish yellow, Cl-green, P-orange, O-red, N-blue, C-grey, H-white.

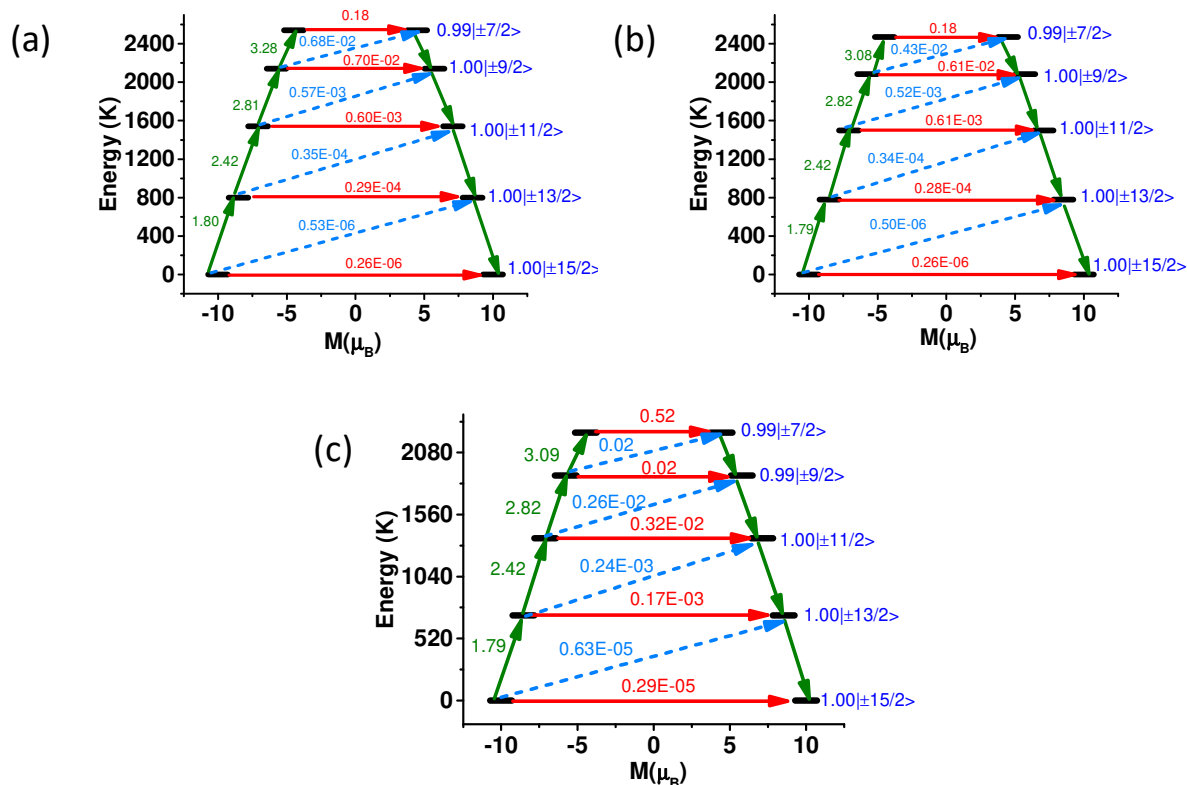


Figure S17. Mechanism of magnetic relaxation of (a) **3a** (b) **4a** (c) **6a**. The red arrows show the QTM and TA-QTM via ground and higher excited KD respectively. The sky dotted arrows show the Orbach process for the relaxation. The green arrows show the mechanism of magnetic relaxation. The blue characters imply the m_j composition of the KDs.

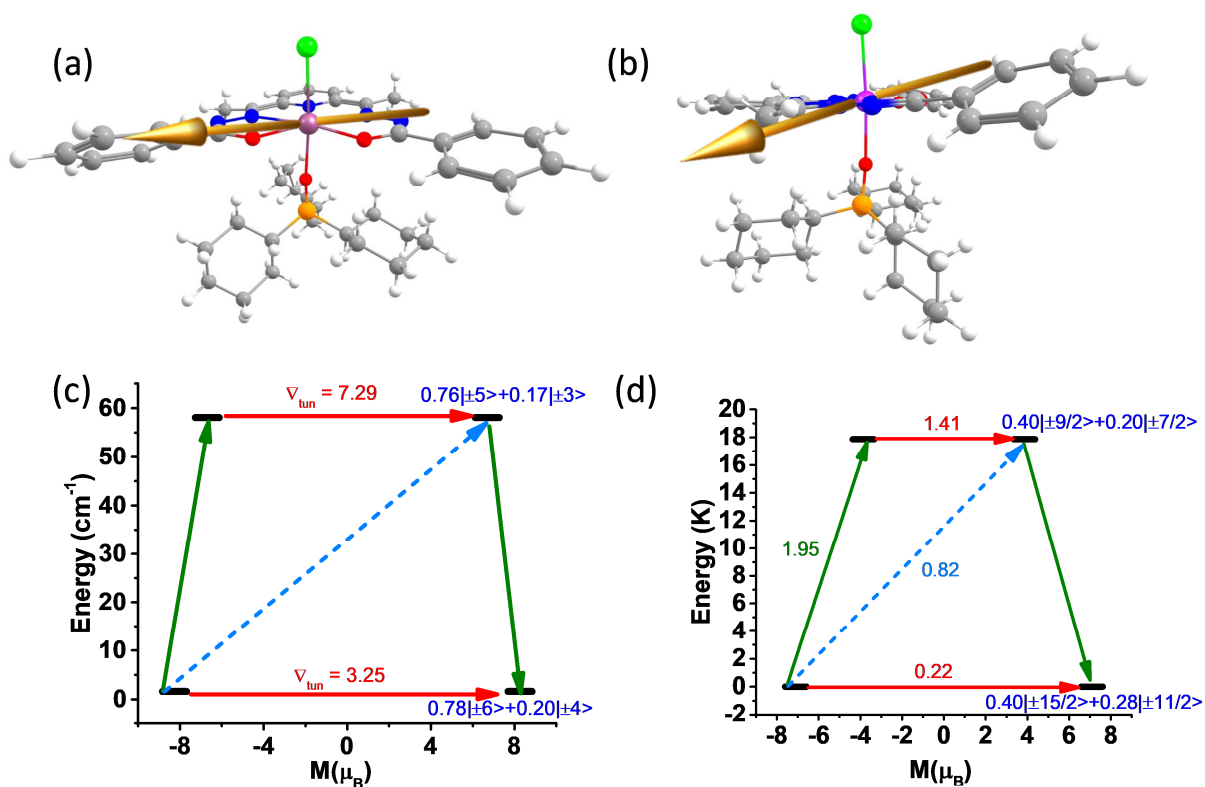


Figure S18. Computed g_{zz} orientation in complex **2** and **5** (a & b) and possible magnetization relaxation pathways (c & d) respectively. Colour code: Er-Pink, Tb-Dark violet, Cl-green, P-orange, O-red, N-blue, C-grey, H-white. The red dotted arrows show the QTM and TA-QTM via ground and higher excited KD respectively. The sky dotted arrows show the Orbach process for the relaxation. The green arrows show the mechanism of magnetic relaxation. The blue characters imply the m_j composition of the KDs.